Journal of Sound and Vibration (2000) **235**(3), 495–520
doi:10.1006/jsvi.2000.2944, available online at http://www.idealibrary.com on IDEAL®

MODELLING SMART STRUCTURES WITH SEGMENTED PIEZOELECTRIC SENSORS AND ACTUATORS

K. Y. Sze and L. Q. Yao†

Department of Mechanical Engineering, The University of Hong Kong Pokfulam Road, Hong Kong SAR, People's Republic of China. E-mail: kysze@hkucc.hku.hk

(*Received* 14 *December* 1999, *and in final form* 7 *March* 2000)

In this paper, a number of finite element models have been developed for comprehensive modelling of smart structures with segmented piezoelectric sensing and actuating patches. These include an eight-node solid-shell element for modelling homogeneous and laminated host structures as well as an eight-node solid-shell and a four-node piezoelectric membrane elements for modelling surface bonded piezoelectric sensing and actuating patches. To resolve the locking problems in these elements and improve their accuracy, assumed natural strain and hybrid stress formulations are employed. Furthermore, piezoelectric patches are often coated with metallization. The concept of electric nodes is introduced that can eliminate the burden of constraining the equality of the electric potential for physical nodes lying on the same metallization. A number of problems are studied by the developed finite element models and comparisons with other *ad hoc* element models are presented.

1. INTRODUCTION

A popular form of smart structure contains a system of piezoelectric sensors which convert the strains of the host structure into electric signals. These signals are fed into microprocessors which in turn activate a system of piezoelectric actuators so that the structure response with respect to external excitations can be altered in real time (see Figure 1). The most widely exploited application of the smart structure technology is active vibration control or active damping. While it is possible to embed the sensors and actuators inside the host structure, segmenatary surface-bonded sensors and actuators are far more popular due to their low fabrication cost.

Designing and analyzing practical smart structures inevitably require the use of finite element method. For this purpose, there have been a number *ad hoc* finite element models developed [1–10]. Owing to the geometric complexity of the surface-bonded sensors and actuators which are most conveniently modelled by continuum elements (no rotational d.o.f.), many of the developed finite element models are continuum in nature [1, 4, 5, 7, 8]. However, strict considerations of locking deficiencies are often lacking in the course of developing these finite element models. It is unfortunate that solid elements when applied to plate and shell analyses can be plagued by the largest number of finite element deficiencies which include shear, membrane, trapezoidal, thickness and dilatational lockings. Thus, solid-to-plate/shell transition elements may have to be adopted whereas excessive aspect ratios of the solid and transition elements must be avoided. Alternatively, transition

† On leave from Department of Mechanics, Lanzhou University, Lanzhou, Gansu 730000, People's Republic of China.

0022-460X/00/330495 + 26 $35.00/0

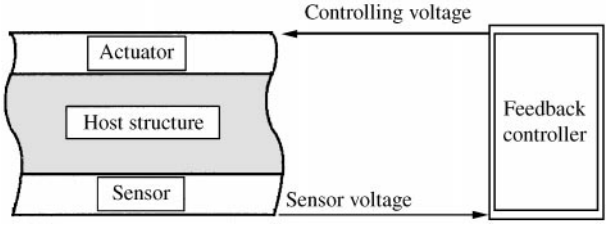

Figure 1. Configuration of a smart structure with sensor and actuator.

elements can be avoided by introducing numerical constraints to tie up the rotations in plate/shell elements with the translations in the solid elements [8]. This practice is tedious and also adversely affects the condition of the system equation.

We shall start with an eight-node element which possesses the same kinetic d.o.f.s as the standard eight-node solid element but is applicable to thin plate/shell analyses without suffering the afore-mentioned lockings. The element is then generalized for modelling piezoelectric materials. Noting that the piezoelectric patch is always coated with metallization which constitutes an equal-potential surface, the concept of electric nodes is introduced that can effectively eliminate the burden of constraining the equality of the electric potential for the nodes lying on the same metallization. A four-node membrane piezoelectric element is also developed that can more efficiently model the piezoelectric patches (e.g., PVDF) which are very thin compared to the host structures. A number of popular examples are considered by the new finite element models to illustrate their accuracy and efficacy in smart structure modelling.

2. GEOMETRIC AND KINEMATIC INTERPOLATION

Figure 2 shows an eight-node hexahedral element in which ξ, η and ζ are the natural co-ordinates. Let ζ be aligned with the transverse direction of the shell, the geometric interpolation can be expressed as

$$\mathbf{X}(\xi, \eta, \zeta) = \sum_{j=1}^{4} N_j(\xi, \eta) \left(\frac{1+\zeta}{2} \mathbf{X}_j^+ + \frac{1-\zeta}{2} \mathbf{X}_j^- \right)$$

$$= (\mathbf{a}_0 + \mathbf{a}_1\xi + \mathbf{a}_2\eta\xi + \mathbf{a}_3\eta) + \zeta(\mathbf{b}_0 + \mathbf{b}_1\xi + \mathbf{b}_2\eta\xi + \mathbf{b}_3\eta) = \mathbf{X}_0 + \zeta\mathbf{X}_n, \qquad (1)$$

where

$$N_1 = (1-\xi)(1-\eta)/4, \qquad N_2 = (1+\xi)(1-\eta)/4, \qquad N_3 = (1+\xi)(1+\eta)/4,$$

$$N_4 = (1-\xi)(1+\eta)/4.$$

$\mathbf{X}$, $\mathbf{X}_j^+$ and $\mathbf{X}_j^-$ are the co-ordinate vectors, its values at the j^+ and j^- nodes of the element

$$\begin{Bmatrix} \mathbf{a}_0 \\ \mathbf{a}_1 \\ \mathbf{a}_2 \\ \mathbf{a}_3 \end{Bmatrix} = \frac{1}{8} \begin{bmatrix} +\mathbf{I}_3 & +\mathbf{I}_3 & +\mathbf{I}_3 & +\mathbf{I}_3 \\ -\mathbf{I}_3 & +\mathbf{I}_3 & +\mathbf{I}_3 & -\mathbf{I}_3 \\ +\mathbf{I}_3 & -\mathbf{I}_3 & +\mathbf{I}_3 & -\mathbf{I}_3 \\ -\mathbf{I}_3 & -\mathbf{I}_3 & +\mathbf{I}_3 & +\mathbf{I}_3 \end{bmatrix} \begin{Bmatrix} \mathbf{X}_1^+ + \mathbf{X}_1^- \\ \mathbf{X}_2^+ + \mathbf{X}_2^- \\ \mathbf{X}_3^+ + \mathbf{X}_3^- \\ \mathbf{X}_4^+ + \mathbf{X}_4^- \end{Bmatrix},$$

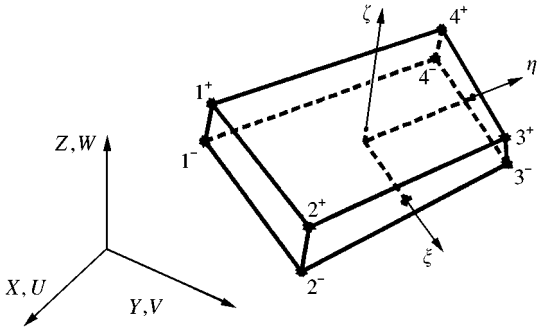

Figure 2. A thin eight-node thin hexahedral solid element.

$$\begin{Bmatrix} \mathbf{b}_0 \\ \mathbf{b}_1 \\ \mathbf{b}_2 \\ \mathbf{b}_3 \end{Bmatrix} = \frac{1}{8} \begin{bmatrix} +\mathbf{I}_3 & +\mathbf{I}_3 & +\mathbf{I}_3 & +\mathbf{I}_3 \\ -\mathbf{I}_3 & +\mathbf{I}_3 & +\mathbf{I}_3 & -\mathbf{I}_3 \\ +\mathbf{I}_3 & -\mathbf{I}_3 & +\mathbf{I}_3 & -\mathbf{I}_3 \\ -\mathbf{I}_3 & -\mathbf{I}_3 & +\mathbf{I}_3 & +\mathbf{I}_3 \end{bmatrix} \begin{Bmatrix} \mathbf{X}_1^+ - \mathbf{X}_1^- \\ \mathbf{X}_2^+ - \mathbf{X}_2^- \\ \mathbf{X}_3^+ - \mathbf{X}_3^- \\ \mathbf{X}_4^+ - \mathbf{X}_4^- \end{Bmatrix}.$$

$\mathbf{I}_m$ is the mth order identity matrix

Similarly, the displacement interpolation can be expressed as

$$\mathbf{U}(\xi, \eta, \zeta) = \sum_{j=1}^{4} N_j(\xi, \eta) \left(\frac{1+\zeta}{2} \mathbf{U}_j^+ + \frac{1-\zeta}{2} \mathbf{U}_j^- \right) = \mathbb{N}(\xi, \eta)\mathbf{q}_0 + \zeta \mathbb{N}(\xi, \eta)\mathbf{q}_n = \mathbf{U}_0 + \zeta \mathbf{U}_n \tag{2}$$

in which

$$\mathbb{N}(\xi, \eta) = [N_1\mathbf{I}_3, N_2\mathbf{I}_3, N_3\mathbf{I}_3, N_4\mathbf{I}_3], \qquad \mathbf{q}_0 = \frac{1}{2} \begin{Bmatrix} \mathbf{U}_1^+ + \mathbf{U}_1^- \\ \mathbf{U}_2^+ + \mathbf{U}_2^- \\ \mathbf{U}_3^+ + \mathbf{U}_3^- \\ \mathbf{U}_4^+ + \mathbf{U}_4^- \end{Bmatrix}, \qquad \mathbf{q}_n = \frac{1}{2} \begin{Bmatrix} \mathbf{U}_1^+ - \mathbf{U}_1^- \\ \mathbf{U}_2^+ - \mathbf{U}_2^- \\ \mathbf{U}_3^+ - \mathbf{U}_3^- \\ \mathbf{U}_4^+ - \mathbf{U}_4^- \end{Bmatrix}.$$

Moreover, $\mathbf{U}$, $\mathbf{U}_j^+$ and $\mathbf{U}_j^-$ are the displacement vectors with respect to the global Cartesian co-ordinates, its values at the j^+ and j^- nodes of the element respectively.

3. ASSUMED NATURAL SHEAR AND THICKNESS STRAINS

In this section, the strain–displacement relation of the element by incorporating the commonly employed geometric assumptions in shells will be presented. With reference to the interpolations of $\mathbf{X}$ and $\mathbf{U}$, the infinitesimal covariant or natural strain components are

$$\varepsilon_\xi = \mathbf{X}_{,\xi}^{\mathrm{T}} \mathbf{U}_{,\xi}, \qquad \varepsilon_\eta = \mathbf{X}_{,\eta}^{\mathrm{T}} \mathbf{U}_{,\eta}, \qquad \gamma_{\xi\eta} = \mathbf{X}_{,\xi}^{\mathrm{T}} \mathbf{U}_{,\eta} + \mathbf{X}_{,\eta}^{\mathrm{T}} \mathbf{U}_{,\xi},$$
$$\varepsilon_\zeta = \mathbf{X}_{,\zeta}^{\mathrm{T}} \mathbf{U}_{,\zeta}, \qquad \gamma_{\zeta\xi} = \mathbf{X}_{,\zeta}^{\mathrm{T}} \mathbf{U}_{,\xi} + \mathbf{X}_{,\xi}^{\mathrm{T}} \mathbf{U}_{,\zeta}, \qquad \gamma_{\zeta\eta} = \mathbf{X}_{,\zeta}^{\mathrm{T}} \mathbf{U}_{,\eta} + \mathbf{X}_{,\eta}^{\mathrm{T}} \mathbf{U}_{,\zeta}. \tag{3}$$

Following the practice in most shell element formulations, the first and second order ζ-terms are truncated in transverse shear strains ($\gamma_{\zeta\xi}$ and $\gamma_{\zeta\eta}$) and the tangential strains (ε_ξ, ε_η

and $\gamma_{\xi\eta}$) respectively. Thus,

$$\varepsilon_\xi = \varepsilon_\xi^m + \zeta\varepsilon_\xi^b, \qquad \varepsilon_\eta = \varepsilon_\eta^m + \zeta\varepsilon_\eta^b, \qquad \varepsilon_\zeta = \mathbf{X}_n^{\mathrm{T}}\mathbb{N}\mathbf{q}_n, \qquad \gamma_{\xi\eta} = \gamma_{\xi\eta}^m + \zeta\gamma_{\xi\eta}^b,$$

$$\gamma_{\zeta\xi} = (\mathbf{b}_0 + \mathbf{b}_1\xi + \mathbf{b}_2\eta\xi + \mathbf{b}_3\eta)^{\mathrm{T}}\,\mathbb{N}_{,\xi}\,\mathbf{q}_0 + (\mathbf{a}_1 + \mathbf{a}_2\eta)^{\mathrm{T}}\,\mathbb{N}\mathbf{q}_n,$$

$$\gamma_{\zeta\eta} = (\mathbf{b}_0 + \mathbf{b}_1\xi + \mathbf{b}_2\eta\xi + \mathbf{b}_3\eta)^{\mathrm{T}}\,\mathbb{N}_{,\eta}\,\mathbf{q}_0 + (\mathbf{a}_3 + \mathbf{a}_2\xi)^{\mathrm{T}}\,\mathbb{N}\mathbf{q}_n \tag{4}$$

in which the membrane "m" and bending "b" strain components can be derived from equations (1) and (2) as

$$\varepsilon_\xi^m = (\mathbf{a}_1 + \mathbf{a}_2\eta)^{\mathrm{T}}\,\mathbb{N}_{,\xi}\,\mathbf{q}_0, \qquad \varepsilon_\xi^b = (\mathbf{b}_1 + \mathbf{b}_2\eta)^{\mathrm{T}}\,\mathbb{N}_{,\xi}\,\mathbf{q}_0 + (\mathbf{a}_1 + \mathbf{a}_2\eta)^{\mathrm{T}}\,\mathbb{N}_{,\xi}\,\mathbf{q}_n,$$

$$\varepsilon_\eta^m = (\mathbf{a}_3 + \xi\mathbf{a}_2)^{\mathrm{T}}\,\mathbb{N}_{,\eta}\,\mathbf{q}_0, \qquad \varepsilon_\eta^b = (\mathbf{b}_3 + \xi\mathbf{b}_2)^{\mathrm{T}}\,\mathbb{N}_{,\eta}\,\mathbf{q}_0 + (\mathbf{a}_3 + \xi\mathbf{a}_2)^{\mathrm{T}}\,\mathbb{N}_{,\eta}\,\mathbf{q}_n,$$

$$\gamma_{\xi\eta}^m = [(\mathbf{a}_1 + \mathbf{a}_2\eta)^{\mathrm{T}}\,\mathbb{N}_{,\eta} + (\mathbf{a}_3 + \xi\mathbf{a}_2)^{\mathrm{T}}\,\mathbb{N}_{,\xi}]\mathbf{q}_0,$$

$$\gamma_{\xi\eta}^b = [(\mathbf{b}_1 + \mathbf{b}_2\eta)^{\mathrm{T}}\,\mathbb{N}_{,\eta} + (\mathbf{b}_3 + \xi\mathbf{b}_2)^{\mathrm{T}}\,\mathbb{N}_{,\xi}]\,\mathbf{q}_0 + [(\mathbf{a}_1 + \mathbf{a}_2\eta)^{\mathrm{T}}\,\mathbb{N}_{,\eta} + (\mathbf{a}_3 + \xi\mathbf{a}_2)^{\mathrm{T}}\,\mathbb{N}_{,\xi}]\,\mathbf{q}_n. \tag{5}$$

As the material properties are often defined in a local orthogonal frame x–y–z, it is necessary to obtain the local physical strains from the covariant ones. It will be assumed as usual that the z-axis and the x–y plane are parallel to the ζ-axis and the mid-surface of the shell respectively. Hence, the relations between the covariant strains and the local physical strains when approximated by the ones evaluated at the mid-surface are [11]

$$\begin{Bmatrix}\varepsilon_x\\ \varepsilon_y\\ \gamma_{xy}\end{Bmatrix} = \begin{bmatrix} x_\xi^2 & x_\eta^2 & 2x_\xi x_\eta \\ y_\xi^2 & y_\eta^2 & 2y_\xi y_\eta \\ x_\xi y_\xi & x_\eta y_\eta & x_\xi y_\eta + x_\eta y_\xi \end{bmatrix}^{-\mathrm{T}} \begin{Bmatrix}\varepsilon_\xi\\ \varepsilon_\eta\\ \gamma_{\xi\eta}\end{Bmatrix}, \qquad \begin{Bmatrix}\gamma_{zx}\\ \gamma_{zy}\end{Bmatrix} = \frac{1}{z_\zeta}\begin{bmatrix} x_\xi & x_\eta \\ y_\xi & y_\eta \end{bmatrix}^{-\mathrm{T}} \begin{Bmatrix}\gamma_{\zeta\xi}\\ \gamma_{\zeta\eta}\end{Bmatrix},$$

$$\varepsilon_z = \frac{1}{z_\zeta^2}\,\varepsilon_\zeta = \frac{1}{\|\,\mathbf{X}_n\,\|^2}\,\varepsilon_\zeta, \tag{6}$$

where

$$x_\xi = \mathbf{e}_x^{\mathrm{T}}\mathbf{X}_{0,\xi}, \qquad y_\xi = \mathbf{e}_y^{\mathrm{T}}\mathbf{X}_{0,\xi}, \qquad x_\eta = \mathbf{e}_x^{\mathrm{T}}\mathbf{X}_{0,\eta}, \qquad y_\eta = \mathbf{e}_y^{\mathrm{T}}\mathbf{X}_{0,\eta}, \qquad z_\zeta = \mathbf{e}_z^{\mathrm{T}}\mathbf{X}_n,$$

in which $\mathbf{e}_x$, $\mathbf{e}_y$ and $\mathbf{e}_z$ are the unit vectors along the local x, y and z directions.

Shear locking is due to the excess number of transverse shear strains sampled in the process of integrating the element stiffness matrix. An effective method of resolving shear locking is the assumed natural strain (ANS) method in which the natural transverse shear strains are interpolated from the ones samples along the element edges. These sampled strains are common to the elements sharing the same edge. Thus, the number of independent shear strains in the system level can be reduced. Following the standard interpolations of four-node ANS shell elements, the natural transverse shear strains are modified to be [12]

$$\tilde{\gamma}_{\zeta\xi} = \frac{1-\eta}{2}\,\gamma_{\zeta\xi}\bigg|_{\xi=0,\,\eta=-1} + \frac{1+\eta}{2}\,\gamma_{\zeta\xi}\bigg|_{\xi=0,\,\eta=+1} \quad \text{and}$$

$$\tilde{\gamma}_{\zeta\eta} = \frac{1-\xi}{2}\,\gamma_{\zeta\eta}\bigg|_{\xi=-1,\,\eta=0} + \frac{1+\xi}{2}\,\gamma_{\zeta\eta}\bigg|_{\xi=+1,\,\eta=0} \tag{7}$$

with which the local Cartesian transverse shear strains $\tilde{\gamma}_{zx}$ and $\tilde{\gamma}_{zy}$ can be obtained by using equation (6).

Another locking phenomenon that plagues solid elements in thin shell analysis is the trapezoidal locking [13]. The strain component leading to the locking is the thickness strain or, equivalently, the normal strain along the thickness direction [14]. ANS can also be adopted to overcome the problem by interpolating the natural thickness strains at the midpoints of the element corners [15], i.e.,

$$\tilde{\varepsilon}_\zeta = N_1 \cdot \varepsilon_\zeta \,|_{\,\xi=-1,\,\eta=-1} + N_2 \cdot \varepsilon_\zeta \,|_{\,\xi=+1,\,\eta=-1} + N_3 \cdot \varepsilon_\zeta \,|_{\,\xi=+1,\,\eta=+1} + N_4 \cdot \varepsilon_\zeta \,|_{\,\xi=-1,\,\eta=+1}\,. \tag{8}$$

By consolidating equation (5) to equation (8), the physical strains can be expressed symbolically as

$$\left\{\begin{matrix}\boldsymbol{\varepsilon}_= \\ \cdots \\ \varepsilon_\parallel\end{matrix}\right\} = \left\{\begin{matrix}\varepsilon_x \\ \varepsilon_y \\ \gamma_{xy} \\ \cdots \\ \tilde{\varepsilon}_z\end{matrix}\right\} = \left\{\begin{matrix}\boldsymbol{\varepsilon}_m + \zeta\boldsymbol{\varepsilon}_b \\ \cdots \\ \varepsilon_\parallel\end{matrix}\right\} = \left[\begin{matrix}\mathbb{B}_m + \zeta\mathbb{B}_b \\ \cdots \\ \mathbb{B}_\parallel\end{matrix}\right]\mathbf{q}^e, \qquad \boldsymbol{\gamma} = \left\{\begin{matrix}\tilde{\gamma}_{zx} \\ \tilde{\gamma}_{zy}\end{matrix}\right\} = \mathbb{B}_t\,\mathbf{q}^e, \tag{9}$$

where $\mathbb{B}$'s are independent of ζ and $\mathbf{q}^e$ is the element displacement vector. Assuming that transverse shear response in uncoupled from the others, the constitutive relation can be expressed as

$$\left\{\begin{matrix}\boldsymbol{\sigma}_= \\ \cdots \\ \sigma_\parallel\end{matrix}\right\} = \left\{\begin{matrix}\sigma_x \\ \sigma_y \\ \tau_{xy} \\ \cdots \\ \sigma_z\end{matrix}\right\} = \left[\begin{matrix}\mathbf{C}_= & \vdots & \mathbf{C}_\times \\ \cdots & \cdots & \cdots \\ \mathbf{C}_\times^{\mathrm{T}} & \vdots & C_\parallel\end{matrix}\right]\left\{\begin{matrix}\varepsilon_x \\ \varepsilon_y \\ \gamma_{xy} \\ \cdots \\ \varepsilon_z\end{matrix}\right\} = \left[\begin{matrix}\mathbf{C}_= & \vdots & \mathbf{C}_\times \\ \cdots & \cdots & \cdots \\ \mathbf{C}_\times^{\mathrm{T}} & \vdots & C_\parallel\end{matrix}\right]\left\{\begin{matrix}\boldsymbol{\varepsilon}_= \\ \cdots \\ \varepsilon_\parallel\end{matrix}\right\}, \qquad \boldsymbol{\tau} = \left\{\begin{matrix}\tau_{zx} \\ \tau_{zy}\end{matrix}\right\} = \mathbf{C}_t\left\{\begin{matrix}\tilde{\gamma}_{zx} \\ \tilde{\gamma}_{zy}\end{matrix}\right\} = \mathbf{C}_t\boldsymbol{\gamma}\,. \tag{10}$$

By adopting the usual approximation of the Jacobian determinant

$$J \approx J_0 = J\,|_{\,\xi=\eta=\zeta=0}\,, \tag{11}$$

the ANS element which is free from shear and trapezoidal locking can be formulated via the following elementwise potential energy functional:

$$\begin{aligned}\Pi_p^e &= \frac{1}{2}\int_{V^e}\left(\left\{\begin{matrix}\boldsymbol{\varepsilon}_= \\ \varepsilon_\parallel\end{matrix}\right\}^{\mathrm{T}}\left[\begin{matrix}\mathbf{C}_= & \vdots & \mathbf{C}_\times \\ \cdots & \cdots & \cdots \\ \mathbf{C}_\times^{\mathrm{T}} & \vdots & C_\parallel\end{matrix}\right]\left\{\begin{matrix}\boldsymbol{\varepsilon}_= \\ \varepsilon_\parallel\end{matrix}\right\} + \boldsymbol{\gamma}^{\mathrm{T}}\mathbf{C}_t\,\boldsymbol{\gamma} - \mathbf{b}^{\mathrm{T}}\mathbf{U}\right)\mathrm{d}v - \int_{S_\sigma^e}\mathbf{t}^{\mathrm{T}}\,\mathbf{U}\mathrm{d}s \\ &= \frac{1}{2}\int_{-1}^{+1}\int_{-1}^{+1}\left(\left\{\begin{matrix}\boldsymbol{\varepsilon}_m \\ \varepsilon_\parallel \\ \boldsymbol{\varepsilon}_b\end{matrix}\right\}^{\mathrm{T}}\mathbf{C}_G\left\{\begin{matrix}\boldsymbol{\varepsilon}_m \\ \varepsilon_\parallel \\ \boldsymbol{\varepsilon}_b\end{matrix}\right\} + \boldsymbol{\gamma}^{\mathrm{T}}\mathbf{C}_T\boldsymbol{\gamma}\right)2J_0\,\mathrm{d}\xi\mathrm{d}\eta - P^e = \frac{1}{2}\,(\mathbf{q}^e)^{\mathrm{T}}\,\mathbb{k}_{ANS}^e\,\mathbf{q}^e - (\mathbf{f}_b^e + \mathbf{f}_\sigma^e)^{\mathrm{T}}\,\mathbf{q}^e,\end{aligned} \tag{12}$$

where

$$\mathbf{C}_G = \frac{1}{2}\int_{-1}^{+1}\left[\begin{matrix}\mathbf{C}_= & \mathbf{C}_\times & \zeta\mathbf{C}_= \\ \mathbf{C}_\times^{\mathrm{T}} & C_\parallel & \zeta C_\times \\ \zeta\mathbf{C}_=^{\mathrm{T}} & \zeta C_\times & \zeta^2\mathbf{C}_=\end{matrix}\right]\mathrm{d}\zeta \quad \text{is the generalized laminate stiffness matrix,}$$

$\mathbf{C}_T = \frac{1}{2}\int_{-1}^{+1} \mathbf{C}_t \, \mathrm{d}\zeta$, V^e denotes the element domain, P^e is the load potential,

$$\mathbb{k}^e_{ANS} = \int_{-1}^{+1}\int_{-1}^{+1} \left(\begin{bmatrix} \mathbb{B}_m \\ \mathbb{B}_{\|} \\ \mathbb{B}_b \end{bmatrix}^{\mathrm{T}} \mathbf{C}_G \begin{bmatrix} \mathbb{B}_m \\ \mathbb{B}_{\|} \\ \mathbb{B}_b \end{bmatrix} + \mathbb{B}_t^{\mathrm{T}} \mathbf{C}_T \mathbb{B}_t \right) 2J_0 \, \mathrm{d}\xi \, \mathrm{d}\eta,$$

$\mathbf{f}^e_b = \int_{V^e} \mathbb{N}^{\mathrm{T}} \mathbf{b} \, \mathrm{d}v$ is the elementwise mechanical force due to the body force $\mathbf{b}$,

$\mathbf{f}^e_\sigma = \int_{S^e_\sigma} \mathbb{N}^{\mathrm{T}} \mathbf{t} \, \mathrm{d}s$ is the elementwise mechanical force due to the surface traction $\mathbf{t}$,

S^e_σ is the portion of the element boundary being prescribed with surface traction.

Moreover, $\mathbf{C}_G$ and $\mathbf{C}_T$ relate the following generalized stresses to the strains $\boldsymbol{\varepsilon}_m$, $\varepsilon_{\|}$, $\boldsymbol{\varepsilon}_b$ and $\boldsymbol{\gamma}$ as

$$\begin{Bmatrix} \mathbf{N} \\ \cdots \\ \mathbf{M} \end{Bmatrix} = \frac{1}{2}\int_{-1}^{+1} \begin{Bmatrix} \boldsymbol{\sigma}_= \\ \sigma_{\|} \\ \cdots \\ \zeta\boldsymbol{\sigma}_= \end{Bmatrix} \mathrm{d}\zeta = \mathbf{C}_G \begin{Bmatrix} \boldsymbol{\varepsilon}_m \\ \varepsilon_{\|} \\ \cdots \\ \boldsymbol{\varepsilon}_b \end{Bmatrix}, \qquad \mathbf{T} = \frac{1}{2}\int_{-1}^{+1} \boldsymbol{\tau} \, \mathrm{d}\zeta = \mathbf{C}_{\mathrm{T}}\boldsymbol{\gamma}. \tag{13}$$

Though the above ANS element is free from shear and trapezoidal locking, it is plagued by thickness locking. In other words, a plane strain conditions instead of the expected plane stress condition will be predicted when the element is loaded by bending moment. The locking phenomenon can be overcome by modifying the generalized laminate stiffness $\mathbf{C}_G$ to $\tilde{\mathbf{C}}_G$ as given in Appendix A.

4. SOLID-SHELL ELEMENT FOR LAMINATED MATERIALS

To apply hybrid stress (HS) formulation to the above ANS solid-shell element as a means to improve the latter's in-plane response, the following elementwise modified Hellinger—Reissner functional can be invoked:

$$\begin{aligned} \Pi^e_{HR} = \int_{V^e} \Bigg(& \frac{-1}{2} \begin{Bmatrix} \mathbf{N} \\ \cdots \\ \mathbf{M} \end{Bmatrix}^{\mathrm{T}} \tilde{\mathbf{C}}_G^{-1} \begin{Bmatrix} \mathbf{N} \\ \cdots \\ \mathbf{M} \end{Bmatrix} + \begin{Bmatrix} \mathbf{N} \\ \cdots \\ \mathbf{M} \end{Bmatrix}^{\mathrm{T}} \begin{Bmatrix} \boldsymbol{\varepsilon}_m \\ \varepsilon_{\|} \\ \cdots \\ \boldsymbol{\varepsilon}_b \end{Bmatrix} - \frac{1}{2}\mathbf{T}^{\mathrm{T}}\mathbf{C}_T^{-1}\mathbf{T} + \mathbf{T}^{\mathrm{T}}\boldsymbol{\gamma} - \mathbf{b}^{\mathrm{T}}\mathbf{U} \Bigg) \mathrm{d}v \\ & - \int_{S^e_\sigma} \mathbf{t}^{\mathrm{T}}\mathbf{U} \, \mathrm{d}s, \end{aligned} \tag{14}$$

The following orthogonal constant and non-constant stress modes are chosen in a way similar to that of Pian's eight-node element [16, 17]:

$$\begin{Bmatrix} \mathbf{N} \\ \cdots \\ \mathbf{M} \end{Bmatrix} = \begin{bmatrix} \mathbf{I}_4 & \mathbf{0}_{4\times 3} & \mathbb{P}_{NH} & \mathbf{0}_{4\times 2} \\ \mathbf{0}_{3\times 4} & \mathbf{I}_3 & \mathbf{0}_{3\times 5} & \mathbb{P}_{MH} \end{bmatrix} \begin{Bmatrix} \boldsymbol{\beta}_{NC} \\ \boldsymbol{\beta}_{MC} \\ \boldsymbol{\beta}_{NH} \\ \boldsymbol{\beta}_{MH} \end{Bmatrix}, \qquad \mathbf{T} = [\mathbf{I}_2 \;\; \mathbb{P}_{TH}] \begin{Bmatrix} \boldsymbol{\beta}_{TC} \\ \boldsymbol{\beta}_{TH} \end{Bmatrix}, \tag{15}$$

where

$$\mathbb{P}_{NH} = \frac{1}{J_0}\begin{bmatrix} \xi\bar{x}_\eta\bar{x}_\eta & 0 & \eta\bar{x}_\xi\bar{x}_\xi & 0 & 0 \\ \xi\bar{y}_\eta\bar{y}_\eta & 0 & \eta\bar{y}_\xi\bar{y}_\xi & 0 & 0 \\ \xi\bar{x}_\eta\bar{y}_\eta & 0 & \eta\bar{x}_\xi\bar{y}_\xi & 0 & 0 \\ 0 & \xi & 0 & \eta & \xi\eta \end{bmatrix}, \qquad \mathbb{P}_{MH} = \frac{1}{J_0}\begin{bmatrix} \xi\bar{x}_\eta\bar{x}_\eta & \eta\bar{x}_\xi\bar{x}_\xi \\ \xi\bar{y}_\eta\bar{y}_\eta & \eta\bar{y}_\xi\bar{y}_\xi \\ \xi\bar{x}_\eta\bar{y}_\eta & \eta\bar{x}_\xi\bar{y}_\xi \end{bmatrix},$$

$$\mathbb{P}_{TH} = \frac{1}{J_0}\begin{bmatrix} \xi\bar{x}_\eta & \eta\bar{x}_\xi \\ \xi\bar{y}_\eta & \eta\bar{y}_\xi \end{bmatrix},$$

$J_0 = J|_{\xi=\eta=\zeta=0}$, $\bar{x}_\xi = x_\xi|_{\xi=\eta=\zeta=0}$, $\bar{y}_\xi = y_\xi|_{\xi=\eta=\zeta=0}$, $\bar{x}_\eta = x_\eta|_{\xi=\eta=\zeta=0}$, $\bar{y}_\eta = y_\eta|_{\xi=\eta=\zeta=0}$.

$\mathbf{0}_{m\times n}$ is the $m\times n$ zero matrix, $\boldsymbol{\beta}$'s are the vectors of stress coefficients.

Adopting the usual approximation in equation (11), the functional can be simplified to

$$\begin{aligned} \Pi^e_{HR} = & -\frac{1}{2}\left(\begin{Bmatrix}\boldsymbol{\beta}_{NC}\\ \boldsymbol{\beta}_{MC}\end{Bmatrix}^{\mathrm{T}} v\tilde{\mathbf{C}}_G^{-1}\begin{Bmatrix}\boldsymbol{\beta}_{NC}\\ \boldsymbol{\beta}_{MC}\end{Bmatrix}^{\mathrm{T}} + \begin{Bmatrix}\boldsymbol{\beta}_{NH}\\ \boldsymbol{\beta}_{MH}\end{Bmatrix}^{\mathrm{T}} \mathbb{H}_G \begin{Bmatrix}\boldsymbol{\beta}_{NH}\\ \boldsymbol{\beta}_{MH}\end{Bmatrix} + \boldsymbol{\beta}_{TC}^{\mathrm{T}} v\mathbf{C}_T^{-1}\boldsymbol{\beta}_{TC} + \boldsymbol{\beta}_{TH}^{\mathrm{T}}\mathbb{H}_T\boldsymbol{\beta}_{TH}\right) \\ & + \left(\begin{Bmatrix}\boldsymbol{\beta}_{NC}\\ \boldsymbol{\beta}_{MC}\end{Bmatrix}^{\mathrm{T}}\begin{bmatrix}\mathbb{G}_{NC}\\ \mathbb{G}_{MC}\end{bmatrix} + \begin{Bmatrix}\boldsymbol{\beta}_{NH}\\ \boldsymbol{\beta}_{MH}\end{Bmatrix}^{\mathrm{T}} + \begin{bmatrix}\mathbb{G}_{NH}\\ \mathbb{G}_{MH}\end{bmatrix} + \boldsymbol{\beta}_{TC}^{\mathrm{T}}\mathbb{G}_{TC} + \boldsymbol{\beta}_{TH}^{\mathrm{T}}\mathbb{G}_{TH}\right)\mathbf{q}^e - (\mathbf{f}_b^e + \mathbf{f}_\sigma^e)^{\mathrm{T}}\mathbf{q}^e, \end{aligned} \tag{16}$$

where

$$v = 2\int_{-1}^{+1}\int_{-1}^{+1} J_0\,\mathrm{d}\xi\,\mathrm{d}\eta, \qquad \mathbb{H}_G = 2\int_{-1}^{+1}\int_{-1}^{+1}\begin{bmatrix}\mathbb{P}_{NH} & \mathbf{0}_{4\times 2}\\ \mathbf{0}_{3\times 5} & \mathbb{P}_{MH}\end{bmatrix}^{\mathrm{T}}\tilde{\mathbf{C}}_G^{-1}\begin{bmatrix}\mathbb{P}_{NH} & \mathbf{0}_{4\times 2}\\ \mathbf{0}_{3\times 5} & \mathbb{P}_{MH}\end{bmatrix} J_0\,\mathrm{d}\xi\,\mathrm{d}\eta,$$

$$\mathbb{H}_T = 2\int_{-1}^{+1}\int_{-1}^{+1}\mathbb{P}_{TH}^{\mathrm{T}}\mathbf{C}_T^{-1}\mathbb{P}_{TH}J_0\,\mathrm{d}\xi\,\mathrm{d}\eta, \qquad \mathbb{G}_{NC} = 2\int_{-1}^{+1}\int_{-1}^{+1}\begin{bmatrix}\mathbb{B}_m\\ \mathbb{B}_\parallel\end{bmatrix}J_0\,\mathrm{d}\xi\,\mathrm{d}\eta,$$

$$\mathbb{G}_{MC} = 2\int_{-1}^{+1}\int_{-1}^{+1}\mathbb{B}_b J_0\,\mathrm{d}\xi\,\mathrm{d}\eta, \qquad \mathbb{G}_{NH} = 2\int_{-1}^{+1}\int_{-1}^{+1}\mathbb{P}_{NH}^{\mathrm{T}}\begin{bmatrix}\mathbb{B}_m\\ \mathbb{B}_\parallel\end{bmatrix}J_0\,\mathrm{d}\xi\,\mathrm{d}\eta,$$

$$\mathbb{G}_{MH} = 2\int_{-1}^{+1}\int_{-1}^{+1}\mathbb{P}_{MH}^{\mathrm{T}}\mathbb{B}_b J_0\,\mathrm{d}\xi\,\mathrm{d}\eta, \qquad \mathbb{G}_{TC} = 2\int_{-1}^{+1}\int_{-1}^{+1}\mathbb{B}_t\,J_0\,\mathrm{d}\xi\,\mathrm{d}\eta,$$

$$\mathbb{G}_{TH} = 2\int_{-1}^{+1}\int_{-1}^{+1}\mathbb{P}_{TH}^{\mathrm{T}}\mathbb{B}_t J_0\,\mathrm{d}\xi\,\mathrm{d}\eta.$$

By invoking the stationary nature of Π^e_{HR} with respect to $\boldsymbol{\beta}$'s, the functional becomes

$$\Pi^e_{HR} = \tfrac{1}{2}(\mathbf{q}^e)^{\mathrm{T}}\,\mathbf{k}^e_{lam}\,\mathbf{q}^e - (\mathbf{f}_b^e + \mathbf{f}_\sigma^e)^{\mathrm{T}}\mathbf{q}^e \tag{17}$$

in which the element stiffness matrix for the HS-ANS element is

$$\mathbb{k}^e_{lam} = \frac{1}{v}\begin{bmatrix}\mathbb{G}_{NC}\\ \mathbb{G}_{MC}\end{bmatrix}^{\mathrm{T}}\tilde{\mathbf{C}}_G\begin{bmatrix}\mathbb{G}_{NC}\\ \mathbb{G}_{MC}\end{bmatrix} + \begin{bmatrix}\mathbb{G}_{NH}\\ \mathbb{G}_{MH}\end{bmatrix}^{\mathrm{T}}\mathbb{H}_G^{-1}\begin{bmatrix}\mathbb{G}_{NH}\\ \mathbb{G}_{MH}\end{bmatrix} + \frac{1}{v}\,\mathbb{G}_{TC}^{\mathrm{T}}\mathbf{C}_T\mathbb{G}_{TC} + \mathbb{G}_{TH}^{\mathrm{T}}\mathbb{H}_T^{-1}\mathbb{G}_{TH}.$$

5. SOLID-SHELL ELEMENT FOR HOMOGENEOUS MATERIALS

If the material is homogeneous instead of laminated, the conventional elementwise Hellinger–Reissner can be employed:

$$\Pi_{HR}^{e} = \int_{V^e} \left(-\frac{1}{2} \begin{Bmatrix} \boldsymbol{\sigma}_{=} \\ \sigma_{\parallel} \end{Bmatrix}^{\mathrm{T}} \mathbf{S}_{\perp} \begin{Bmatrix} \boldsymbol{\sigma}_{=} \\ \sigma_{\parallel} \end{Bmatrix} - \frac{1}{2} \boldsymbol{\tau}^{\mathrm{T}} \mathbf{S}_t \boldsymbol{\tau} + \begin{Bmatrix} \boldsymbol{\sigma}_{=} \\ \sigma_{\parallel} \end{Bmatrix}^{\mathrm{T}} \begin{Bmatrix} \boldsymbol{\varepsilon}_{=} \\ \varepsilon_{\parallel} \end{Bmatrix} + \boldsymbol{\tau}^{\mathrm{T}} \boldsymbol{\gamma} - \mathbf{b}^{\mathrm{T}} \mathbf{U} \right) \mathrm{d}v - \int_{S_\sigma^e} \mathbf{t}^{\mathrm{T}} \mathbf{U} \, \mathrm{d}s, \tag{18}$$

where

$$\mathbf{S}_{\perp} = \left[\begin{array}{c:c} \mathbf{S}_{=} & \mathbf{S}_{\times} \\ \hdashline \mathbf{S}_{\times}^{\mathrm{T}} & S_{\parallel} \end{array}\right] = \left[\begin{array}{c:c} \mathbf{C}_{=} & \mathbf{C}_{\times} \\ \hdashline \mathbf{C}_{\times}^{\mathrm{T}} & C_{\parallel} \end{array}\right]^{-1} = \mathbf{C}_{\perp}^{-1}.$$

Analogous to the laminated element, the assumed stress field is taken to be

$$\begin{Bmatrix} \boldsymbol{\sigma}_{=} \\ \sigma_{\parallel} \end{Bmatrix} = \left[\begin{array}{c:c:c:c} \mathbf{I}_4 & \mathbb{P}_{NH} & \boldsymbol{\zeta}\mathbf{I}_3 & \boldsymbol{\zeta}\mathbb{P}_{MH} \\ & & \mathbf{0}_{1\times 3} & \mathbf{0}_{1\times 2} \end{array}\right] \begin{Bmatrix} \boldsymbol{\beta}_{NC} \\ \boldsymbol{\beta}_{NH} \\ \boldsymbol{\beta}_{MC} \\ \boldsymbol{\beta}_{MH} \end{Bmatrix}, \qquad \boldsymbol{\tau} = [\mathbf{I}_2 \;\; \mathbb{P}_{TH}] \begin{bmatrix} \boldsymbol{\beta}_{TC} \\ \boldsymbol{\beta}_{TH} \end{bmatrix}. \tag{19}$$

By substituting equations (9) and (19) into the functional, the latter becomes

$$\begin{aligned} \Pi_{HR}^{e} = -\frac{1}{2} \Bigg(& v\boldsymbol{\beta}_{NC}^{\mathrm{T}} \mathbf{S}_{\perp} \boldsymbol{\beta}_{NC} + \boldsymbol{\beta}_{NH}^{T} \mathbb{H}_{NH} \boldsymbol{\beta}_{NH}^{\mathrm{T}} + \frac{v}{3} \boldsymbol{\beta}_{MC}^{\mathrm{T}} \mathbf{S}_{=} \boldsymbol{\beta}_{MC} + \frac{1}{3} \boldsymbol{\beta}_{MH}^{\mathrm{T}} \mathbb{H}_{MH} \boldsymbol{\beta}_{MH}^{\mathrm{T}} + v\boldsymbol{\beta}_{TC}^{\mathrm{T}} \mathbf{S}_t \boldsymbol{\beta}_{TC} \\ & + \boldsymbol{\beta}_{TH}^{\mathrm{T}} \mathbb{H}_{TH} \boldsymbol{\beta}_{TH}^{T} \Bigg) + \Bigg(\boldsymbol{\beta}_{NC}^{\mathrm{T}} \mathbb{G}_{NC} + \boldsymbol{\beta}_{NH}^{\mathrm{T}} \mathbb{G}_{NH} + \frac{1}{3} \boldsymbol{\beta}_{MC}^{\mathrm{T}} \mathbb{G}_{MC} + \frac{1}{3} \boldsymbol{\beta}_{MH}^{\mathrm{T}} \mathbb{G}_{MH} + \boldsymbol{\beta}_{TC}^{\mathrm{T}} \mathbb{G}_{TC} \\ & + \boldsymbol{\beta}_{TH}^{\mathrm{T}} \mathbb{G}_{TH} \Bigg) \mathbf{q}^{e} - (\mathbf{f}_b^{e} + \mathbf{f}_\sigma^{e})^{\mathrm{T}} \mathbf{q}^{e}. \end{aligned} \tag{20}$$

By invoking the stationary nature of Π_{HR}^{e} with respect to $\boldsymbol{\beta}$'s, the following HS-ANS element stiffness matrix is obtained:

$$\begin{aligned} \mathbb{k}_{\mathrm{hom}}^{e} = & \frac{1}{v} \mathbb{G}_{NC}^{\mathrm{T}} \mathbf{C}_{\perp} \mathbb{G}_{NC} + \frac{1}{3v} \mathbb{G}_{MC}^{\mathrm{T}} \mathbf{S}_{=}^{-1} \mathbb{G}_{MC} + \frac{1}{v} \mathbb{G}_{TC}^{\mathrm{T}} \mathbf{C}_t \mathbb{G}_{TC} \\ & + \mathbb{G}_{NH}^{\mathrm{T}} \mathbb{H}_{NH}^{-1} \mathbb{G}_{NH} + \frac{1}{3} \mathbb{G}_{MH}^{\mathrm{T}} \mathbb{H}_{MH}^{-1} \mathbb{G}_{MH} + \mathbb{G}_{TH}^{\mathrm{T}} \mathbb{H}_{TH}^{-1} \mathbb{G}_{TH}, \end{aligned} \tag{21}$$

where the undefined matrices are

$$\mathbb{H}_{NH} = 2 \int_{-1}^{+1} \int_{-1}^{+1} \mathbb{P}_{NH}^{\mathrm{T}} \mathbf{S}_{\perp} \mathbb{P}_{NH} J_0 \, \mathrm{d}\xi \mathrm{d}\eta, \qquad \mathbb{H}_{MH} = 2 \int_{-1}^{+1} \int_{-1}^{+1} \mathbb{P}_{MH}^{\mathrm{T}} \mathbf{S}_{=} \mathbb{P}_{MH} J_0 \, \mathrm{d}\xi \mathrm{d}\eta,$$

$$\mathbb{H}_{TH} = 2 \int_{-1}^{+1} \int_{-1}^{+1} \mathbb{P}_{TH}^{\mathrm{T}} \mathbf{S}_t \mathbb{P}_{TH} J_0 \, \mathrm{d}\xi \mathrm{d}\eta.$$

As a matter of fact, the element stiffness can also be degenerated from equation (17) by noting that

$$\tilde{\mathbf{C}}_G = \begin{bmatrix} \mathbf{C}_= & \mathbf{C}_\times & \mathbf{0}_{3\times 3} \\ \mathbf{C}_\times^{\mathrm{T}} & C_\parallel & \mathbf{0}_{1\times 3} \\ \mathbf{0}_{3\times 3} & \mathbf{0}_{3\times 1} & \mathbf{S}_=^{-1}/3 \end{bmatrix} \tag{22}$$

for homogeneous materials (see Appendix A).

6. SOLID-SHELL ELEMENT FOR PIEZOELECTRIC PATCHES

Piezoelectric patches used for surfaced-bonded segmentary sensors and actuators are always coated with metallization such as printed silver ink. Compared to the overall thickness of the patches, the metallization thickness can be ignored. Hence, the metallization is not separately modelled in the piezoelectric element models. The presence of metallization induces two equal-potential surfaces coincident with the top and bottom surfaces of the patches. In this section, the afore-derived hybrid-HS-ANS solid-shell element will be generalized for modelling the piezoelectric patches and for taking into account the equipotential surfaces.

For generic piezoelectric solid elements, each node is equipped with three translations and electric potential as the nodal d.o.f.s. It would be necessary to constrain the equality of the electric d.o.f.s. of the nodes on the same metallization. To avoid this tedious task, the electric d.o.f.s are separated from the kinetic nodes with which kinetic d.o.f.s. are associated. The electric node has two d.o.f.s which are the two electric potentials ϕ_{TOP} and ϕ_{BOTTOM} on the upper and lower metallizations. Unlike kinetic nodes, electric nodes have no co-ordinates. For instance, Figure 3 shows two elements that model the same piezoelectric patch and they only need two electric d.o.f.s which are grouped under the electric node "p". Under the present ways of arranging the nodal d.o.f.s, their connectivities are [a, c, j, h, b, d, k, i, p] and [c, f, m, j, d, g, n, k, p]. The first eight nodes are kinetic nodes and the last nodes are electric nodes. The interpolated electric potential is

$$\phi = \frac{1}{2}\,[1+\zeta \;\; 1-\zeta] \begin{Bmatrix} \phi_{TOP} \\ \phi_{BOTTOM} \end{Bmatrix} = \frac{1}{2}\,[1+\zeta \;\; 1-\zeta]\,\mathbf{\Phi}^e. \tag{23}$$

With respect to the local Cartesian co-ordinates defined in section 3, the electric field can be approximated as

$$\mathbf{E} = \begin{Bmatrix} E_x \\ E_y \\ E_z \end{Bmatrix} = \begin{Bmatrix} 0 \\ 0 \\ -\phi_{,z} \end{Bmatrix} \quad \text{and} \quad E_z = E_\parallel = -\phi_{,z} = -\frac{1}{2\,\|\,\mathbf{X}_n\,\|}\,[+1 \;\; -1] \begin{Bmatrix} \phi_{TOP} \\ \phi_{BOTTOM} \end{Bmatrix} = -\mathbb{B}_e\mathbf{\Phi}^e. \tag{24}$$

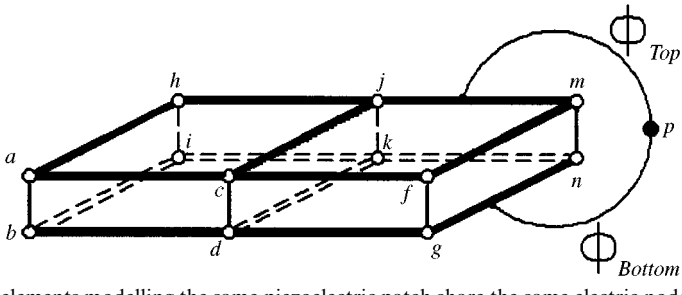

Figure 3. Solid elements modelling the same piezoelectric patch share the same electric node. Connectivities of the elements are [a, c, j, h, b, k, i, p] and [c, f, m, j, d, g, n, k, p].

Within two of the electric field components having vanished and the pooling direction always aligned with the transverse direction, the piezoelectric constructive relation can be expressed as

$$\begin{Bmatrix} \boldsymbol{\sigma}_{=} \\ \sigma_{\parallel} \\ \cdots\cdots \\ \boldsymbol{\tau} \\ D_{\parallel} \end{Bmatrix} = \left[\begin{array}{c:c:c} \mathbf{C}_{\perp} & \mathbf{0}_{4\times 2} & -\mathbf{e}_{\perp}^{\mathrm{T}} \\ \hdashline \mathbf{0}_{2\times 4} & \mathbf{C}_{t} & \mathbf{0}_{2\times 1} \\ \mathbf{e}_{\perp} & \mathbf{0}_{1\times 2} & \in_{\parallel} \end{array}\right] \begin{Bmatrix} \boldsymbol{\varepsilon}_{=} \\ \varepsilon_{\parallel} \\ \cdots\cdots \\ \boldsymbol{\gamma} \\ E_{\parallel} \end{Bmatrix} \tag{25}$$

in which $\mathbf{e}_{\perp} = [e_{31} \quad e_{32} \quad e_{36} \quad e_{33}]$ contains the piezo-strain coefficients, $D_{\parallel}$ and $\in_{\parallel} = \in_{33}$ are respectively, the electric displacement and the permittivity coefficient in the transverse direction. By changing the object of the equation,

$$\begin{Bmatrix} \boldsymbol{\varepsilon}_{=} \\ \varepsilon_{\parallel} \\ \cdots\cdots \\ \boldsymbol{\gamma} \\ D_{\parallel} \end{Bmatrix} = \left[\begin{array}{c:c:c} \mathbf{C}_{\perp}^{-1} & \mathbf{0}_{4\times 2} & \mathbf{C}_{\perp}^{-1}\mathbf{e}_{\perp}^{\mathrm{T}} \\ \hdashline \mathbf{0}_{2\times 4} & \mathbf{C}_{t}^{-1} & \mathbf{0}_{2\times 1} \\ \mathbf{e}_{\perp}\mathbf{C}_{\perp}^{-1} & \mathbf{0}_{1\times 2} & \in_{\parallel} + \mathbf{e}_{\perp}\mathbf{C}_{\perp}^{-1}\mathbf{e}_{\perp}^{\mathrm{T}} \end{array}\right] \begin{Bmatrix} \boldsymbol{\sigma}_{=} \\ \sigma_{\parallel} \\ \boldsymbol{\tau} \\ E_{\parallel} \end{Bmatrix} = \left[\begin{array}{c:c:c} \mathbf{S}_{\perp} & \mathbf{0}_{4\times 2} & \mathbf{d}_{\perp}^{\mathrm{T}} \\ \hdashline \mathbf{0}_{2\times 4} & \mathbf{S}_{t} & \mathbf{0}_{2\times 1} \\ \mathbf{d}_{\perp} & \mathbf{0}_{1\times 2} & \varsigma_{\parallel} \end{array}\right] \begin{Bmatrix} \boldsymbol{\sigma}_{=} \\ \sigma_{\parallel} \\ \cdots\cdots \\ \boldsymbol{\tau} \\ E_{\parallel} \end{Bmatrix} \tag{26}$$

in which the entries in $\mathbf{d}_{\perp} = [d_{31} \; d_{32} \; d_{36} \; d_{33}]$ are known as the piezo-stress coefficients and $\varsigma_{\parallel} = \varsigma_{33}$ is the dielectric coefficient in the transverse direction. To formulate a solid-shell element for piezoelectric patch, the following elementwise hybrid function is invoked [18, 19]:

$$\Pi^{e} = \int_{V^{e}} \left(-\frac{1}{2} \begin{Bmatrix} \boldsymbol{\sigma}_{=} \\ \sigma_{\parallel} \\ \cdots\cdots \\ \boldsymbol{\tau} \\ -E_{\parallel} \end{Bmatrix}^{\mathrm{T}} = \left[\begin{array}{c:c:c} \mathbf{S}_{\perp} & \mathbf{0}_{4\times 2} & -\mathbf{d}_{\perp}^{\mathrm{T}} \\ \hdashline \mathbf{0}_{2\times 4} & \mathbf{S}_{t} & \mathbf{0}_{2\times 1} \\ -\mathbf{d}_{\perp} & \mathbf{0}_{1\times 2} & \varsigma_{\parallel} \end{array}\right] \begin{Bmatrix} \boldsymbol{\sigma}_{=} \\ \sigma_{\parallel} \\ \cdots\cdots \\ \boldsymbol{\tau} \\ -E_{\parallel} \end{Bmatrix} + \begin{Bmatrix} \boldsymbol{\sigma}_{=} \\ \sigma_{\parallel} \\ \boldsymbol{\tau} \end{Bmatrix}^{\mathrm{T}} \begin{Bmatrix} \boldsymbol{\varepsilon}_{=} \\ \varepsilon_{\parallel} \\ \boldsymbol{\gamma} \end{Bmatrix} - \mathbf{b}^{\mathrm{T}}\mathbf{U} \right) \mathrm{d}v$$

$$- \int_{S_{\sigma}^{e}} \mathbf{t}^{\mathrm{T}}\mathbf{U}\,\mathrm{d}s + \int_{S_{Q}^{e}} Q\phi\,\mathrm{d}s, \tag{27}$$

where S_{Q}^{e} is the portion of the element boundary being prescribed with the charge density Q. By invoking equations (9), (11), (19) and (24), we have

$$\begin{aligned} \Pi^{e} = & -\frac{v}{2}\boldsymbol{\beta}_{NC}^{\mathrm{T}}\mathbf{S}_{\perp}\boldsymbol{\beta}_{NC} - \frac{1}{2}\boldsymbol{\beta}_{NH}^{\mathrm{T}}\mathbb{H}_{NH}\boldsymbol{\beta}_{NH}^{\mathrm{T}} - \frac{v}{2}\boldsymbol{\beta}_{TC}^{\mathrm{T}}\mathbf{S}_{t}\boldsymbol{\beta}_{TC} - \frac{1}{2}\boldsymbol{\beta}_{TH}^{\mathrm{T}}\mathbb{H}_{TH}\boldsymbol{\beta}_{TH}^{\mathrm{T}} - \frac{v}{6}\boldsymbol{\beta}_{MC}^{\mathrm{T}}\mathbf{S}_{=}\boldsymbol{\beta}_{MC} \\ & - \frac{1}{6}\boldsymbol{\beta}_{MH}^{\mathrm{T}}\mathbb{H}_{MH}\boldsymbol{\beta}_{MH}^{\mathrm{T}} + \frac{1}{3}\boldsymbol{\beta}_{MC}^{\mathrm{T}}\mathbb{G}_{MC}\mathbf{q}^{e} + \frac{1}{3}\boldsymbol{\beta}_{MH}^{\mathrm{T}}\mathbb{G}_{MH}\mathbf{q}^{e} + \boldsymbol{\beta}_{TC}^{\mathrm{T}}\mathbb{G}_{TC}\mathbf{q}^{e} + \boldsymbol{\beta}_{TH}^{\mathrm{T}}\mathbb{G}_{TH}\mathbf{q}^{e} \\ & - \frac{1}{2}(\boldsymbol{\Phi}^{e})^{\mathrm{T}}\mathbb{A}\boldsymbol{\Phi}^{e} + \boldsymbol{\beta}_{NC}^{\mathrm{T}}\left[\mathbb{G}_{NC} \;\; \mathbb{E}_{C}\right]\begin{Bmatrix} \mathbf{q}^{e} \\ \boldsymbol{\Phi}^{e} \end{Bmatrix} + \boldsymbol{\beta}_{NH}^{\mathrm{T}}\left[\mathbb{G}_{NH} \;\; \mathbb{E}_{H}\right]\begin{Bmatrix} \mathbf{q}^{e} \\ \boldsymbol{\Phi}^{e} \end{Bmatrix} - \begin{Bmatrix} \mathbf{f}_{b}^{e} + \mathbf{f}_{\sigma}^{e} \\ \mathbf{f}_{Q}^{e} \end{Bmatrix}^{\mathrm{T}}\begin{Bmatrix} \mathbf{q}^{e} \\ \boldsymbol{\Phi}^{e} \end{Bmatrix}, \end{aligned} \tag{28}$$

where the undefined terms are

$$\mathbb{E}_{C} = 2\int_{-1}^{+1}\int_{-1}^{+1} \mathbf{d}_{\perp}^{\mathrm{T}}\mathbb{B}_{e}J_{0}\,\mathrm{d}\xi\mathrm{d}\eta, \qquad \mathbb{E}_{H} = 2\int_{-1}^{+1}\int_{-1}^{+1} \mathbb{P}_{NH}^{\mathrm{T}}\mathbf{d}_{\perp}^{\mathrm{T}}\mathbb{B}_{e}J_{0}\,\mathrm{d}\xi\mathrm{d}\eta,$$

$$\mathbb{A} = 2\int_{-1}^{+1}\int_{-1}^{+1} \varsigma_{\|}\,\mathbb{B}_e^{\mathrm{T}}\mathbb{B}_e J_0 \,\mathrm{d}\xi\mathrm{d}\eta,$$

$$\mathbf{f}_Q^e = -\begin{Bmatrix} Q_{TOP}\,A_{TOP} \\ Q_{BOTTOM}\,A_{BOTTOM} \end{Bmatrix} \quad \text{is the elementwise electric force vector.}$$

Moreover, A_{TOP} and A_{BOTTOM} are, respectively, the areas of the upper and lower element surfaces whereas Q_{TOP} and Q_{BOTTOM} are, respectively, the prescribed charge densities, if any, at the upper and lower element surfaces. After condensing $\boldsymbol{\beta}$'s with the stationary conditions of Π^e with respect to $\boldsymbol{\beta}$'s, the functional can be expressed as

$$\Pi^e = \frac{1}{2}\begin{Bmatrix}\mathbf{q}^e \\ \boldsymbol{\Phi}^e\end{Bmatrix}^{\mathrm{T}}\begin{bmatrix}\mathbb{k}_{mm}^e & \mathbb{k}_{me}^e \\ (\mathbb{k}_{me}^e)^{\mathrm{T}} & \mathbb{k}_{ee}^e\end{bmatrix}\begin{Bmatrix}\mathbf{q}^e \\ \boldsymbol{\Phi}^e\end{Bmatrix} - \begin{Bmatrix}\mathbf{f}_b^e + \mathbf{f}_\sigma^e \\ \mathbf{f}_Q^e\end{Bmatrix}^{\mathrm{T}}\begin{Bmatrix}\mathbf{q}^e \\ \boldsymbol{\Phi}^e\end{Bmatrix} \tag{29}$$

in which

$$\mathbb{k}_{mm}^e = \mathbb{k}_{hom}^e, \qquad \mathbb{k}_{me}^e = \frac{1}{v}\,\mathbb{G}_{NC}^{\mathrm{T}}\mathbf{C}_\perp\mathbb{E}_C + \mathbb{G}_{NH}^{\mathrm{T}}\,\mathbb{H}_{NH}^{-1}\mathbb{E}_H, \qquad \mathbb{k}_{ee}^e = \frac{1}{v}\,\mathbb{E}_C^{\mathrm{T}}\mathbf{C}_\perp\mathbb{E}_C + \mathbb{E}_H^{\mathrm{T}}\,\mathbb{H}_{NH}^{-1}\mathbb{E}_H - \mathbb{A}\,.$$

It should be remarked that higher computational efficiency can be obtained by block-diagonalizing the flexibility submatrices $\mathbb{H}$'s in the context of the admissible matrix formulation [17].

7. MEMBRANE ELEMENT FOR PIEZOELECTRIC THIN PATCHES

When the thickness of piezoelectric patches is much less than that of the host structure (e.g., the typical thickness of PVDF thin films in $20 \sim 100\ \mu$m), the piezoelectric patches can be modelled more efficiently by membrane elements whose bending and transverse shear stiffness are negligible and ignored. This section will derive a membrane element by degenerating the solid-shell element presented in section 6, (see Figure 4). The element has four kinetic nodes and one electric node. Each of the kinetic nodes is equipped with three translation d.o.f.s. The geometric and displacement interpolations are

$$\mathbf{X}(\xi,\eta) = \sum_{i=1}^{4} N_i(\xi,\eta)\mathbf{X}_i, \qquad \mathbf{U}(\xi,\eta) = \sum_{i=1}^{4} N_i(\xi,\eta)\,\mathbf{U}_i. \tag{30}$$

From equations (5) and (6), the in-plane membrane strain can be expressed as

$$\boldsymbol{\varepsilon}_= = \begin{bmatrix}\varepsilon_x \\ \varepsilon_y \\ \gamma_{xy}\end{bmatrix} = \begin{bmatrix} x_\xi^2 & x_\eta^2 & 2x_\xi x_\eta \\ y_\xi^2 & y_\eta^2 & 2y_\xi y_\eta \\ x_\xi y_\xi & x_\eta y_\eta & x_\xi y_\eta + x_\eta y_\xi\end{bmatrix}^{-\mathrm{T}}\begin{Bmatrix}\mathbf{X}_{,\xi}^{\mathrm{T}}\,\mathbf{U}_{,\xi} \\ \mathbf{X}_{,\eta}^{\mathrm{T}}\,\mathbf{U}_{,\eta} \\ \mathbf{X}_{,\xi}^{\mathrm{T}}\,\mathbf{U}_{,\eta} + \mathbf{X}_{,\eta}^{\mathrm{T}}\mathbf{U}_{,\xi}\end{Bmatrix} = \mathbb{B}_=\mathbf{q}^e \tag{31}$$

and the electric field component transverse to the element is

$$E_{\|} = -\frac{\phi_{TOP} - \phi_{BOTTOM}}{t} = -\frac{1}{t}\,[1,-1]\begin{Bmatrix}\phi_{TOP} \\ \phi_{BOTTOM}\end{Bmatrix} = -\,\mathbb{B}_e\,\boldsymbol{\Phi}^e \tag{32}$$

in which t denotes the thickness. With $E_x = E_y = \sigma_{\|} = \tau_{zx} = \tau_{zy} = 0$, the constitutive relation in equation (26) can be simplified as

$$\begin{Bmatrix}\boldsymbol{\varepsilon}_= \\ D_{\|}\end{Bmatrix} = \begin{bmatrix}\mathbf{S}_= & \mathbf{d}_=^{\mathrm{T}} \\ \mathbf{d}_= & \varsigma_{\|}\end{bmatrix}\begin{Bmatrix}\boldsymbol{\sigma}_= \\ E_{\|}\end{Bmatrix}, \tag{33}$$

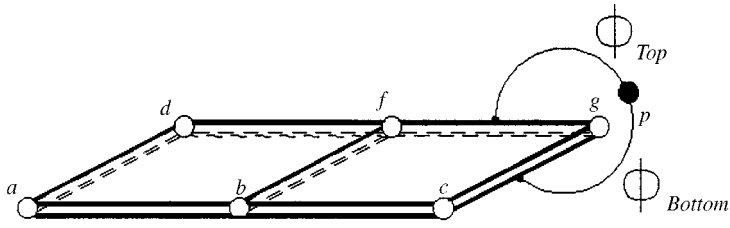

Figure 4. Membrane elements modelling the same piezoelectric film share the same electric node. Connectivities for the elements are [a, d, f, d, p] and [b, c, g, f, p].

where $\mathbf{d}_=$ contains only the first three entries of $\mathbf{d}_\perp$. The two-dimensional counterpart of the functional in equation (27) is

$$\begin{aligned}\Pi^e &= \int_{V^e}\left(-\frac{1}{2}\begin{Bmatrix}\boldsymbol{\sigma}_= \\ -E_\parallel\end{Bmatrix}^{\mathrm{T}}\begin{bmatrix}\mathbf{S}_= & -\mathbf{d}_=^{\mathrm{T}} \\ -\mathbf{d}_= & \varsigma_\parallel\end{bmatrix}\begin{Bmatrix}\boldsymbol{\sigma}_= \\ -E_\parallel\end{Bmatrix} + \boldsymbol{\sigma}_=^{\mathrm{T}}\boldsymbol{\varepsilon}_= - \mathbf{b}^{\mathrm{T}}\mathbf{U}\right)\mathrm{d}v - \int_{S_\sigma^e}\mathbf{t}^{\mathrm{T}}\mathbf{U}\,\mathrm{d}s + \int_{S_Q^e} Q\phi\,\mathrm{d}s \\ &= \int_{-1}^{+1}\int_{-1}^{+1}\left(-\frac{1}{2}\begin{Bmatrix}\boldsymbol{\sigma}_= \\ -E_\parallel\end{Bmatrix}^{\mathrm{T}}\begin{bmatrix}\mathbf{S}_= & -\mathbf{d}_=^{\mathrm{T}} \\ -\mathbf{d}_= & \varsigma_\parallel\end{bmatrix}\begin{Bmatrix}\boldsymbol{\sigma}_= \\ -E_\parallel\end{Bmatrix} + \boldsymbol{\sigma}_=^{\mathrm{T}}\boldsymbol{\varepsilon}_= - \mathbf{b}^{\mathrm{T}}\mathbf{U}\right)J\,\mathrm{d}\xi\,\mathrm{d}\eta \\ &\quad - \int_{S_\sigma^e}\mathbf{t}^{\mathrm{T}}\mathbf{U}\,\mathrm{d}s + \int_{S_Q^e} Q\phi\,\mathrm{d}s,\end{aligned} \tag{34}$$

where $J = t\,\|\,\mathbf{X}_{,\xi}\times\mathbf{X}_{,\eta}\,\|$. The assumed stress is degenerated from equation (19) is

$$\boldsymbol{\sigma}_= = \boldsymbol{\beta}_C + \mathbb{P}_H\boldsymbol{\beta}_H = \boldsymbol{\beta}_C + \frac{1}{J}\begin{bmatrix}\xi\bar{x}_\eta\bar{x}_\eta & \eta\bar{x}_\xi\bar{x}_\xi \\ \xi\bar{y}_\eta\bar{y}_\eta & \eta\bar{y}_\xi\bar{y}_\xi \\ \xi\bar{x}_\eta\bar{y}_\eta & \eta\bar{x}_\xi\bar{y}_\xi\end{bmatrix}\boldsymbol{\beta}_H, \tag{35}$$

With equations (31), (32) and (35) substituted into equation (34), the latter can be written as

$$\begin{aligned}\Pi^e = &-\frac{v}{2}\boldsymbol{\beta}_C^{\mathrm{T}}\mathbf{S}_=\boldsymbol{\beta}_C - \frac{1}{2}\boldsymbol{\beta}_H^{\mathrm{T}}\mathbb{H}_H\boldsymbol{\beta}_H^{\mathrm{T}} + \boldsymbol{\beta}_C^{\mathrm{T}}\begin{bmatrix}\mathbb{G}_C & \mathbb{E}_C\end{bmatrix}\begin{Bmatrix}\mathbf{q}^e \\ \boldsymbol{\Phi}^e\end{Bmatrix} + \boldsymbol{\beta}_H^{\mathrm{T}}\begin{bmatrix}\mathbb{G}_H & \mathbb{E}_H\end{bmatrix}\begin{Bmatrix}\mathbf{q}^e \\ \boldsymbol{\Phi}^e\end{Bmatrix} \\ &- \frac{1}{2}(\boldsymbol{\Phi}^e)^{\mathrm{T}}\,\mathbb{A}\boldsymbol{\Phi}^e - \begin{Bmatrix}\mathbf{f}_b^e + \mathbf{f}_\sigma^e \\ \mathbf{f}_Q^e\end{Bmatrix}^T\begin{Bmatrix}\mathbf{q}^e \\ \boldsymbol{\Phi}^e\end{Bmatrix}.\end{aligned} \tag{36}$$

After condensing $\boldsymbol{\beta}$'s with the stationary conditions of Π^e with respect to $\boldsymbol{\beta}$'s, the functional of the present element can also be expressed in the same form as equation (29) except that

$$\begin{aligned}&\mathbb{k}_{mm}^e = \frac{1}{v}\mathbb{G}_C^{\mathrm{T}}\mathbf{S}_=^{-1}\mathbb{G}_C + \mathbb{G}_H^{\mathrm{T}}\mathbb{H}_H^{-1}\mathbb{G}_H, \qquad \mathbb{k}_{me}^e = \frac{1}{v}\mathbb{G}_C^{\mathrm{T}}\mathbf{S}_=^{-1}\mathbb{E}_C + \mathbb{G}_H^{\mathrm{T}}\mathbb{H}_H^{-1}\mathbb{E}_H, \\ &\mathbb{k}_{ee}^e = \frac{1}{v}\mathbb{E}_C^{\mathrm{T}}\mathbf{S}_=^{-1}\mathbb{E}_C + \mathbb{E}_H^{\mathrm{T}}\mathbb{H}_H^{-1}\mathbb{E}_H - \mathbb{A}\end{aligned} \tag{37}$$

in which

$$\begin{aligned}&v = \int_{V^e}\mathrm{d}v = \int_{-1}^{+1}\int_{-1}^{+1}J\,\mathrm{d}\xi\,\mathrm{d}\eta, \qquad \mathbb{G}_C = \int_{-1}^{+1}\int_{-1}^{+1}\mathbb{B}_=\,J\,\mathrm{d}\xi\,\mathrm{d}\eta, \\ &\mathbb{G}_H = \int_{-1}^{+1}\int_{-1}^{+1}\mathbb{P}_H^{\mathrm{T}}\mathbb{B}_=\,J\,\mathrm{d}\xi\,\mathrm{d}\eta, \qquad \mathbb{H}_H = \int_{-1}^{+1}\int_{-1}^{+1}\mathbb{P}_H^{\mathrm{T}}\mathbf{S}_=\mathbb{P}_H\,J\,\mathrm{d}\xi\,\mathrm{d}\eta,\end{aligned}$$

$$\mathbb{E}_C = \int_{-1}^{+1}\int_{-1}^{+1} \mathbf{d}_{=}^{\mathrm{T}}\,\mathbb{B}_e\,J\,\mathrm{d}\xi\,\mathrm{d}\eta, \qquad \mathbb{E}_H = \int_{-1}^{+1}\int_{-1}^{+1} \mathbb{P}_H^{\mathrm{T}}\mathbf{d}_{=}^{\mathrm{T}}\,\mathbb{B}_e\,J\,\mathrm{d}\xi\,\mathrm{d}\eta,$$

$$\mathbb{A} = \int_{-1}^{+1}\int_{-1}^{+1} \varsigma_{\|}\,\mathbb{B}_e^{\mathrm{T}}\mathbb{B}_e J\,\mathrm{d}\xi\,\mathrm{d}\eta.$$

Lastly, it should be remarked that the membrane element is rank deficient and can only be used as an adherent to solid elements.

8. SYSTEM EQUATION AND EIGENANALYSIS

After summing all the elementwise functional Π^e and taking the variation of nodal displacements and electric potential, the system equation can be expressed as

$$\begin{bmatrix} \mathbb{K}_{mm} & \mathbb{K}_{me} \\ \mathbb{K}_{me}^{\mathrm{T}} & \mathbb{K}_{ee} \end{bmatrix} \begin{Bmatrix} \mathbf{q} \\ \mathbf{\Phi} \end{Bmatrix} = \begin{Bmatrix} \mathbf{F}_b + \mathbf{F}_\sigma \\ \mathbf{F}_Q \end{Bmatrix} \tag{38}$$

in which $\mathbb{K}$'s are assembled from the element matrices $\mathbb{k}$'s, $\mathbf{q}$ and $\mathbf{\Phi}$ are the system vectors of nodal displacements and electric potentials, respectively, $\mathbf{F}_b$, $\mathbf{F}_\sigma$ and $\mathbf{F}_Q$ are the assembled counterparts of $\mathbf{f}_b^e$, $\mathbf{f}_\sigma^e$ and $\mathbf{f}_Q^e$ respectively. For dynamic analysis, the inertia and damping forces can be accounted for in terms of the body force, i.e.,

$$\mathbf{F}_b = -\mathbb{M}\ddot{\mathbf{q}} - \mathbb{C}\dot{\mathbf{q}} = -\mathbb{M}\ddot{\mathbf{q}} - (\alpha\mathbb{M} + \beta\mathbb{K}_{mm})\,\dot{\mathbf{q}} \tag{39}$$

in which α and β are the Rayleigh's damping coefficients, $\mathbb{M}$ is the mass matrix assembled from $\int_{V^e}\rho\mathbb{N}^{\mathrm{T}}\mathbb{N}\,\mathrm{d}v$ and ρ is the mass density. Thus, the system equation can be expanded as

$$\begin{bmatrix} \mathbb{M} & \mathbf{0} \\ \mathbf{0} & \mathbf{0} \end{bmatrix} \begin{Bmatrix} \ddot{\mathbf{q}} \\ \ddot{\mathbf{\Phi}} \end{Bmatrix} + \begin{bmatrix} \mathbb{C} & \mathbf{0} \\ \mathbf{0} & \mathbf{0} \end{bmatrix} \begin{Bmatrix} \dot{\mathbf{q}} \\ \dot{\mathbf{\Phi}} \end{Bmatrix} + \begin{bmatrix} \mathbb{K}_{mm} & \mathbb{K}_{me} \\ \mathbb{K}_{me}^{\mathrm{T}} & \mathbb{K}_{ee} \end{bmatrix} \begin{Bmatrix} \mathbf{q} \\ \mathbf{\Phi} \end{Bmatrix} = \begin{Bmatrix} \mathbf{F}_\sigma \\ \mathbf{F}_Q \end{Bmatrix}. \tag{40}$$

Natural frequencies and their mode shapes can be obtained by setting the right-hand side vector to zero and condensing $\mathbf{\Phi}$ with $\mathbf{\Phi} = -\mathbb{K}_{ee}^{-1}\mathbb{K}_{me}^{\mathrm{T}}\mathbf{q}$.

9. ACTIVE CONTROL OF SMART STRUCTURES

Figure 1 shows a typical configuration of smart structure with piezoelectric sensors and actuators. The sensors sense the strains of the host structure and produce electrical potentials. The signals are fed into controllers which implement certain control algorithms. Outputs of the controllers are used to strain the actuators which in turn strain the host structure. By partitioning the system vector of electric potential $\mathbf{\Phi}$ into that of the actuators $\mathbf{\Phi}^A$ and of the sensors $\mathbf{\Phi}^S$, equation (40) can be split into

$$\mathbb{M}\ddot{\mathbf{q}} + \mathbb{C}\dot{\mathbf{q}} + \mathbb{K}_{mm}\mathbf{q} + \mathbb{K}_{me}^A\mathbf{\Phi}^A + \mathbb{K}_{me}^S\mathbf{\Phi}^S = \mathbf{F}_\sigma, \quad \begin{Bmatrix} \mathbf{\Phi}^A \\ \mathbf{\Phi}^S \end{Bmatrix} = \begin{bmatrix} (\mathbb{K}_{ee}^A)^{-1} & \mathbf{0} \\ \mathbf{0} & (\mathbb{K}_{ee}^S)^{-1} \end{bmatrix} \left(\begin{Bmatrix} \mathbf{F}_Q^A \\ \mathbf{F}_Q^S \end{Bmatrix} - \begin{bmatrix} (\mathbb{K}_{me}^A)^{\mathrm{T}} \\ (\mathbb{K}_{me}^S)^{\mathrm{T}} \end{bmatrix} \mathbf{q} \right), \tag{41}$$

where

$$\begin{Bmatrix} \mathbf{\Phi}^A \\ \mathbf{\Phi}^S \end{Bmatrix} = \mathbf{\Phi}, \qquad \begin{bmatrix} (\mathbb{K}_{ee}^A)^{-1} & \mathbf{0} \\ \mathbf{0} & (\mathbb{K}_{ee}^S)^{-1} \end{bmatrix} = \mathbb{K}_{ee}^{-1}, \qquad [\mathbb{K}_{me}^A,\ \mathbb{K}_{me}^S] = \mathbb{K}_{me}, \qquad \begin{Bmatrix} \mathbf{F}_Q^A \\ \mathbf{F}_Q^S \end{Bmatrix} = \mathbf{F}_Q.$$

In particular, $\mathbb{K}_{ee}$ is the block diagonal because the host structure is non-piezoelectric, i.e., $\mathbf{\Phi}^A$ and $\mathbf{\Phi}^S$ do not couple. As there is no electric loading applied to the sensors, $\mathbf{F}_Q^S$ vanished. Consequently, equation (41) gives

$$\mathbf{\Phi}^S = -(\mathbb{K}_{ee}^S)^{-1}(\mathbb{K}_{me}^S)^{\mathrm{T}}\,\mathbf{q} \tag{42}$$

which gives sensor outputs and can be processed to provide input signals to the actuators for active vibration control. Substitution of equation (42) into equation (41) results in

$$\mathbb{M}\ddot{\mathbf{q}} + \mathbb{C}\dot{\mathbf{q}} + [\mathbb{K}_{mm} - \mathbb{K}_{me}^S(\mathbb{K}_{ee}^S)^{-1}(\mathbb{K}_{me}^S)^{\mathrm{T}}]\,\mathbf{q} = \mathbf{F}_\sigma - \mathbb{K}_{me}^A\,\mathbf{\Phi}^A. \tag{43}$$

With the control algorithm known and by virtue of equation (43), $\mathbf{\Phi}_A$ can be expressed in terms of $\mathbf{q}$ and thus all the electric d.o.f.s. in equation (43) can be condensed.

For active dampling, negative velocity feedback can be adopted as the control algorithm with which $\mathbf{\Phi}^S$ and $\mathbf{\Phi}^A$ can be related by a control gain matrix $\mathbb{T}_\phi$, namely,

$$\mathbf{\Phi}^A = -\mathbb{T}_\phi\,\dot{\mathbf{\Phi}}^S. \tag{44}$$

With equation (42), equations (43) and (44) become

$$\mathbf{\Phi}^A = \mathbb{T}_\phi(\mathbb{K}_{ee}^S)^{-1}(\mathbb{K}_{me}^S)^{\mathrm{T}}\dot{\mathbf{q}}, \qquad \mathbb{M}\ddot{\mathbf{q}} + (\mathbb{C} + \bar{\mathbb{C}})\dot{\mathbf{q}} + \mathbb{K}\mathbf{q} = \mathbf{F}_\sigma, \tag{45}$$

where

$$\bar{\mathbb{C}} = \mathbb{K}_{me}^A\,\mathbb{T}_\phi(\mathbb{K}_{ee}^S)^{-1}(\mathbb{K}_{me}^S)^{\mathrm{T}}, \qquad \mathbb{K} = \mathbb{K}_{mm} - \mathbb{K}_{me}^S(\mathbb{K}_{ee}^S)^{-1}(\mathbb{K}_{me}^S)^{\mathrm{T}}.$$

Matrices $\mathbb{C}$ and $\bar{\mathbb{C}}$ will be termed as passive and active damping matrices which are due to material dissipation and active damping effect of the smart structure respectively.

By means of modal analysis, the global displacement $\mathbf{q}$ can be expressed in terms of the vector of modal generalized displacements $\boldsymbol{\theta}$ as

$$\mathbf{q} = \mathbb{Y}\boldsymbol{\theta} \tag{46}$$

in which $\mathbb{Y} = (\mathbf{\Psi}_1, \mathbf{\Psi}_2, \ldots, \mathbf{\Psi}_i, \ldots]$ is the square matrix that contained all the normalized eigenvectors $\mathbf{\Psi}_i$'s of the undamped system as its column vectors, i.e.,

$$(\mathbb{K} - \omega_i^2\,\mathbb{M})\mathbf{\Psi}_i = \mathbf{0}, \tag{47}$$

where ω_i is the eigenvalue pertinent to $\mathbf{\Psi}_i$. Substituting equation (46) into equation (45) and multiplying the latter with the transpose of $\mathbf{\Psi}$, we have

$$\mathbb{Y}^{\mathrm{T}}\mathbb{M}\mathbb{Y}\ddot{\boldsymbol{\theta}} + \mathbb{Y}^{\mathrm{T}}(\mathbb{C} + \bar{\mathbb{C}})\mathbb{Y}\dot{\boldsymbol{\theta}} + \mathbb{Y}^{\mathrm{T}}\mathbb{K}\mathbb{Y}\boldsymbol{\theta} = \mathbb{Y}^{\mathrm{T}}\mathbf{F}_\sigma. \tag{48}$$

By using the orthonormal property of the modal matrix, the above equation can be simplified as

$$\ddot{\boldsymbol{\theta}} + (\mathrm{diag}\,\{2\mu_1\omega_1, \ldots, 2\mu_i\omega_i, \ldots,\} + \mathbb{Y}^{\mathrm{T}}\bar{\mathbb{C}}\mathbb{Y})\dot{\boldsymbol{\theta}} + diag\,\{\omega_1^2, \ldots, \omega_i^2, \ldots\}\,\boldsymbol{\theta} = \mathbb{Y}^{\mathrm{T}}\mathbf{F}_\sigma \tag{49}$$

in which $\mu_i = (\alpha + \beta\omega_i^2)/(2\omega_i)$ is the *passive damping ratio* arising from the Rayleigh's damping. In case of $\mathbb{Y}^{\mathrm{T}}\bar{\mathbb{C}}\mathbb{Y}$ being diagonal, the system response can be solved by the classical mode superposition method. In particular, if only the first-mode is considered, the governing equation can be reduced from equation (49) as

$$\ddot{\theta}_1 + 2(\mu_1 + \bar{\mu}_1)\omega_1\dot{\theta}_1 + \omega_1^2\theta_1 = 0, \tag{50}$$

where $\bar{\mu}_1$ is the *active damping ratio* induced by the control algorithm and is equal to the (1, 1)-entry of $\mathbb{Y}^{\mathrm{T}}\bar{\mathbb{C}}\mathbb{Y}$ divided by $2\omega_1$.

10. NUMERICAL EXAMPLES

In this section, a number of problem related to smart structure modelling are studied by the elements derived in sections 4–7. The adhesive in between the host structures and the piezoelectric patches will be assumed to be thin enough to be neglected. Thus, the concept of using viscoelastic constraint layers for passive damping will not be studied.

10.1 BIMORPH POINTER

A bimorph pointer is portrayed in Figure 5. It consists of two identical PVDF layers ($E = 2$ GPa, $\nu = 0{\cdot}29$, $e_{31} = e_{32} = 0{\cdot}046$ C/m^2, $\epsilon_{33} = 0{\cdot}1062$ nF/m) with vertical but opposite polarities and, hence, will bend when an electric field is applied vertically. The bimorph is modelled by 2×5 elements. With a unit voltage applied across the thickness, the deflection of bimorph beam is computed by the present piezoelectric solid-shell element and compared with the theoretical and other finite element predictions as listed in Table 1. It can be seen that the present solid-shell element model matches theoretical results up to four significant figures.

The tip deflection of the bimorph is the prescribed to 1 cm and the open circuit voltage output across the thickness is computed. Figure 6 shows the predicted voltage when 1, 5 and 10 electrode (metallization) pairs are employed. The related meshes contain 2×5, 2×5 and 2×10 elements. The predictions show excellent agreement with the analytical solution [20] in which the equipotential effect induced by the metallization is ignored and thus the electric potential is a continuous function of x.

The effect of mesh distortion on the element accuracy is then studied. The bimorph is modelled by 2×4 elements as shown in Figure 7. With a unit voltage applied across the thickness, the free end deflection is computed by the present element and the following piezoelectric solid elements in ABAQUS [21]:

- C3D8E—the 8-node piezoelectric brick element.
- C3D20ER—the 20-node reduced integrated piezoelectric brick element.

Using the beam theory in which a plane stress condition is assumed in the Y direction, the analytical end deflection is 0·345 μm. To assess the element accuracy by the beam solution, the Poisson ratio is set to zero for mimicking the required plane stress condition. The

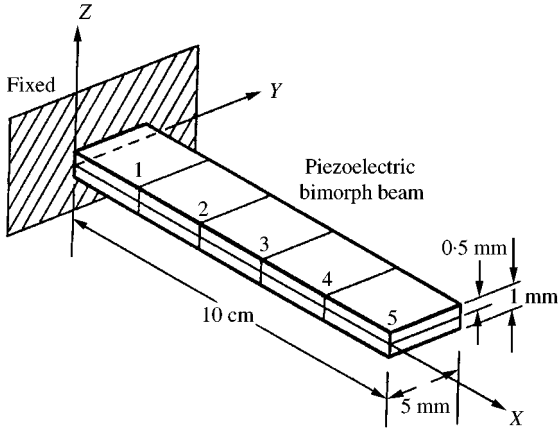

Figure 5. A bimorph cantilever modelled by 2×5 elements.

TABLE 1

Static deflection of the piezoelectric bimorph beam (10^{-7} m), *see Figure* 5

Distance x (mm)	20	40	60	80	100
Tseng† [10]	0·150	0·569	1·371	2·351	3·598
Tzou† [20]	0·124	0·508	1·16	2·10	3·30
Tzou and Ye† [7]	0·132	0·528	1·19	2·11	3·30
Wang *et al.* [9]	0·139	0·547	1·135	2·198	3·416
Detwiler *et al.*	0·14	0·55	1·24	2·21	3·45
Analytical [20]	0·138	0·552	1·242	2·208	3·450
Present†	0·138	0·552	1·242	2·208	3·450

† The element derived are solid or solid shell elements.

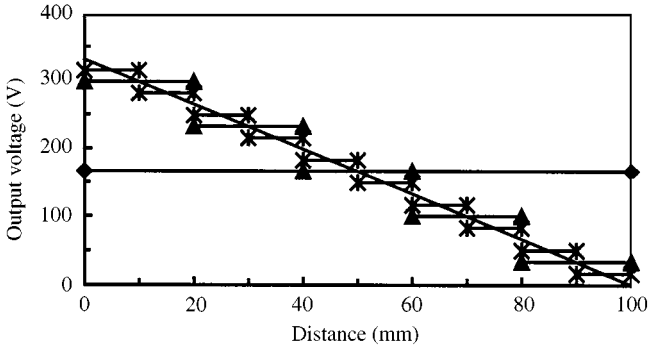

Figure 6. Convergence of sensor voltage for a prescribed tip deflection (see Figure 5): —◆— 1-electrode; —▲— 5-electrodes; —✳— 10-electrodes; —— analytical [20].

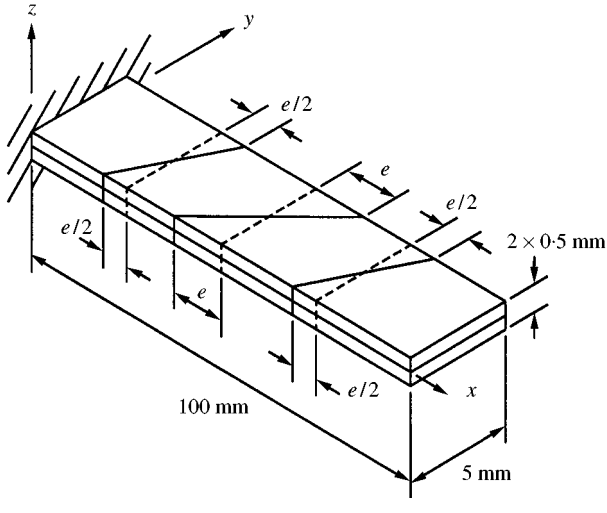

Figure 7. The bimorph cantilever model led by 2×4 distorted elements.

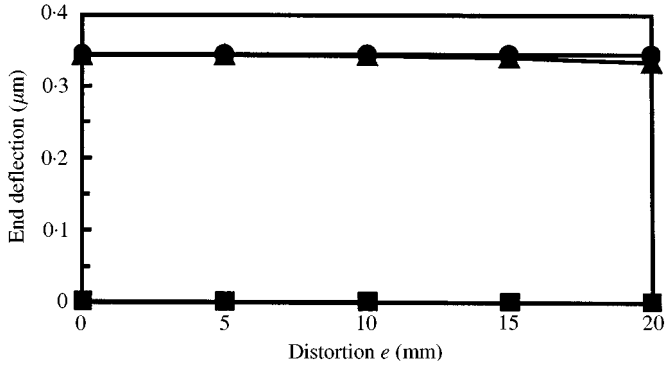

Figure 8. End deflections versus distortion for the bimorph cantilever problem (see Figure 7): —●— present/reference; —▲— C3D20ER; —■— C3D8E.

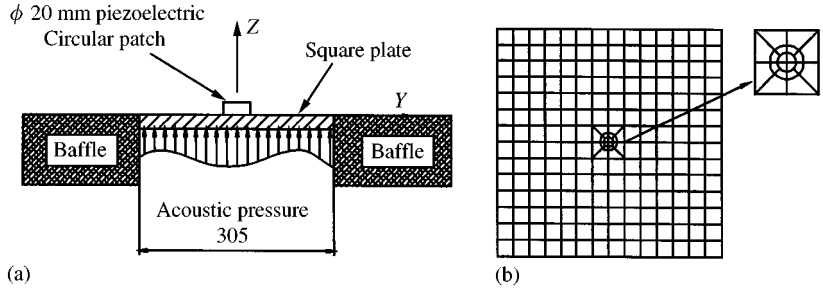

Figure 9. (a) A clamped square aluminum plate with a circular PZT patch. (b) The employed mesh.

predicted end deflections for different element distortions "e" are plotted in Figure 8. Without resorting to any advanced finite element technique, C3D8E is very poor in accuracy. Despite the higher order nature of C3D20ER, its accuracy is marginally lower than that of the present element whose prediction is graphically indistinguishable from the beam solutions.

10.2. ALUMINUM SQUARE PLATE WITH A CIRCULAR PIEZOELECTRIC WAFER

Figure 9 shows a $305 \times 305 \times 0{\cdot}8$ mm fully clamped aluminum square plate ($\rho = 2800$ kg/m^3, $E = 68$ GPa, $\nu = 0{\cdot}32$) with a $\phi 20$ mm piezoelectric wafer bonded to its centre. The wafer is 1 mm thick and made of PZT-5H ($\rho = 7500$ kg/m^3, $E_1 = E_2 = 62{\cdot}5$ GPa, $E_3 = 57{\cdot}16$ GPa, $G_{44} = G_{55} = 23$ GPa, $G_{66} = 23{\cdot}3$ GPa, $\nu_{12} = 0{\cdot}3345$, $\nu_{13} = \nu_{23} = 0{\cdot}442$, $e_{31} = e_{32} = -6{\cdot}5$ C/m^2, $e_{33} = 23{\cdot}3$ C/m^2, $\epsilon_{33} = 13$ nF/m). A 1 Pa uniform pressure is applied to the lower surface of the plate. The mesh layout is essentially the same as the one used by Kim *et al.* [8] who employed 192 nine-node flat shell, 8 thirteen-node solid-to-plate transition, 4 twenty-node solid and 4 twenty-node piezoelectric solid elements [8]. In the present analysis, 200 solid-shell and 12 piezoelectric solid-shell elements are employed. The static central deflections with and without the wafer are listed in Table 2. Given the high accuracy of the result in the absence of the wafer and the relative dimension of the plate and the wafer (area ratio $\approx 300:1$), the predicted deflection of Kim *et al.* appears to be too small. It is noteworthy that the ratio of the active d.o.f.s in

TABLE 2

Static central deflection for the clamped square aluminum plate, see Figure 9

	Without wafer (μm)	With wafer (μm)
Kim *et al.* [8]	Not available	2·465
Present	3·381	3·253
Series solution [23]	3·380	Not available

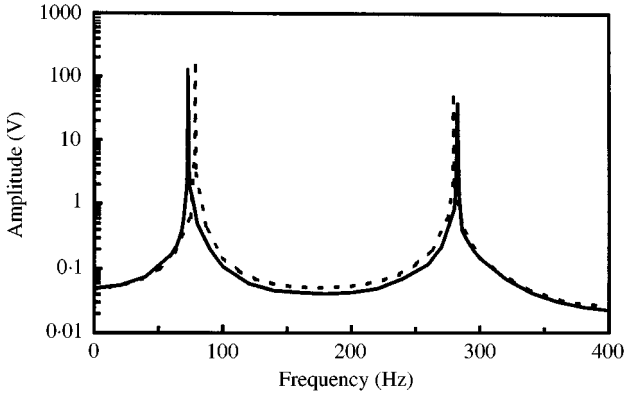

Figure 10. Sensor response of aluminum square plate under pressure loading (see Figure 9): - - - - Kim *et al.* [8]; ——— present.

Kim *et al*'s mesh and the present one is $\approx 3:1$, not to mention the modelling burden of co-using four different types of elements.

Figure 10 shows the peak voltage output of the wafer when the plate is subjected to sinusoidal pressure loading. The first two peaks predicted by the present elements are 74·20 and 284·16 Hz whereas the predictions of Kim *et al.* [8] are 78·5 and 279·5 Hz. The differences in the first and second peaks are $\approx 5\%$ and $\approx 4\%$. In the absence of the piezoelectric wafer, series solutions [22] and the predictions of the present element for the first two symmetric eigenmodes are 74·06/270·0 and 74·81/290·0 Hz respectively. The difference in the first eigenfrequency is $\approx 1\%$. It should be remarked that the voltage does not peak at the unsymmetric eigenmode in which the centre of plate is stationary.

10.3. CANTILEVER COMPOSITE PLATE WITH DISTRIBUTED ACTUATORS

Figure 11 shows a composite cantilever plate with 22 square and eight non-square surface-bonded G-1195 piezoelectric ceramic patches ($\rho = 7600\ \text{kg/m}^3$, $E = 63{\cdot}0$ GPa, $G = 24{\cdot}2$ GPa, $\nu = 0{\cdot}3$, $d_{31} = d_{32} = 254$ pm/V, $d_{33} = 374$ pm/V, $d_{24} = 584$ pm/V, $\varsigma_{11} = \varsigma_{22} = 15{\cdot}3$ nF/m, $\varsigma_{33} = 15{\cdot}0$ nF/m). Stacking of the composite plate is $[0^\circ/\pm 45^\circ]$s and the plate is made of T300/976 graphite/epoxy unidirectional laminae ($\rho = 1600\ \text{kg/m}^3$, $E_L = 150$ GPa, $E_T = 9$ GPa, $G_{TL} = 7{\cdot}1$ GPa, $G_{TT} = 2{\cdot}5$ GPa, $\nu_{LT} = \nu_{TT} = 0{\cdot}3$). Following the mesh of Ha *et al.* [1], the host plate is modelled by 10×16 elements. A voltage supply of 157·6 V is applied to the piezoelectric patches such that the ones above and below the

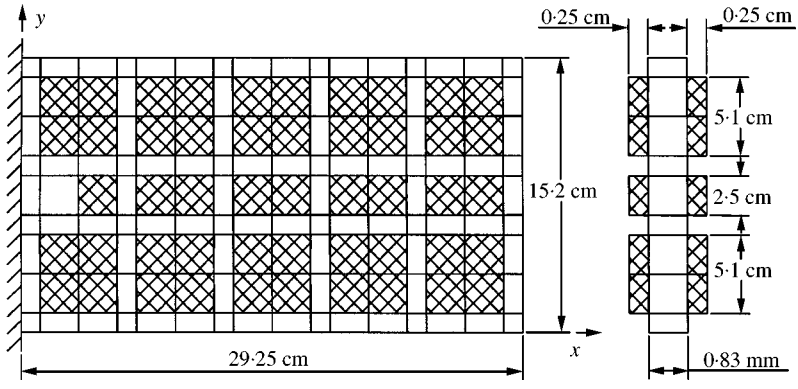

Figure 11. A cantilever composite plate with 30 surface-bonded piezoelectric actuators.

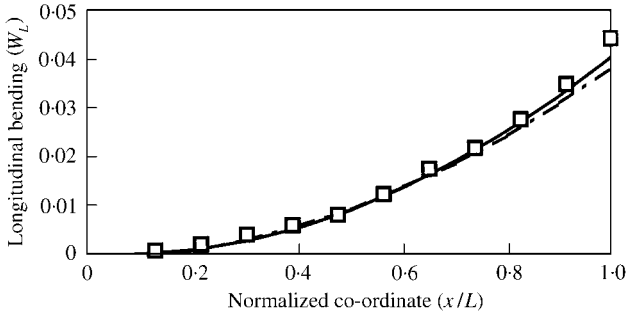

Figure 12. Non-dimensional longitudinal bending deflection of the cantilever plate in Figure 11: ——— Present; – – – – Ha *et al.* [1]; □ experiment [24].

composite plate are subjected to equal but opposite electric fields of magnitude 394 V/mm. The following non-dimensional deflection parameters are computed by the present element models and shown in Figures 12–14:

$$W_L = \frac{W|_{y=7{\cdot}6\text{ cm}}}{C}, \qquad W_T = \frac{W|_{y=7{\cdot}6\text{ cm}} - (W|_{y=15{\cdot}2\text{ cm}} + W|_{y=0\text{ cm}})/2}{C} \quad \text{and}$$

$$W_R = \frac{W|_{y=15.2\text{ cm}} - W|_{y=0\text{ cm}}}{C}$$

which correspond to longitudinal bending, transverse bending and lateral twisting deflections. In the above equations, $C = 15{\cdot}2$ cm is the width of the plate. For the purpose of comparison the experimental results of Crawly and Lazarus [24] and the finite element predictions of Ha *et al.* [1] are also included in the figures. The element models developed by Ha *et al.* are eight-node solid elements with nine incompatible displacement modes. These incompatible elements suffer from shear locking when the elements are not in the form of rectangular prisms [25]. Despite the regular geometry of the elements in this example, W_R perdicted by the incompatible models are apparently smaller than that obtained by the present models and the experimental measurement.

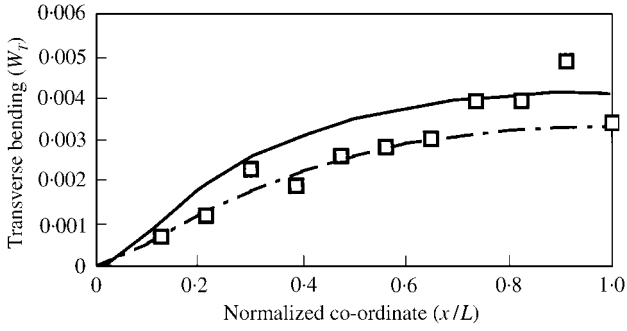

Figure 13. Non-dimensional transverse bending deflection of the cantilever plate in Figure 11: ——— Present; - - - - Ha *et al.* [1]; □ experiment [24].

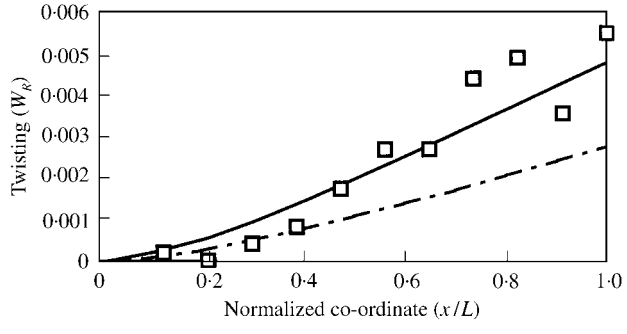

Figure 14. Non-dimensional lateral twisting deflection of the cantilever plate in Figure 11: ——— Present; - - - - Ha *et al.* [1]; □ experiment [24].

10.4. STEEL RING WITH SEGMENTED SENSORS AND ACTUATORS

Figure 15 shows a 6·35 mm thick semi-circular steel ring ($\rho = 7750\,\text{kg/m}^3$, $E = 68{\cdot}95\,\text{GPa}$, $\nu = 0{\cdot}3$) sandwiched by two PZT layers ($\rho = 7600\,\text{kg/m}^3$, $E = 63\,\text{GPa}$, $\nu = 0{\cdot}3$, $d_{31} = 179\,\text{pm/V}$, $\in_{33} = 16{\cdot}50\,\text{nF/m}$). The thickness of the PZT layers is taken to be either 254 or 50·8 μm.

In the absence of the PZT layers, the lowest eigenfrequencies of the steel ring are computed and listed in Table 3. For the purpose of comparison predictions of the following ABAQUS [21] curved shells.

- S4—the 4-node general-purpose (thin and thick) shell element,
- S4R5—a stabilized reduced-integrated 4-node thin shell element with 5 d.o.f. per node,
- S9R5—a stabilized reduced-integrated 9-node thin shell element with 5 d.o.f. per node,

as well as Tzou and Ye's 12-node triangular prismatic solid element [7] are also included. The predictions of S4 and the present solid-shell element are insensitive to the mesh density. This implies that the mesh densities have been adequate for the two-element models to give reasonably converged results. With 1×10 elements, predicted frequencies of S4R5 are very low. The observation is probably due to the hourglass modes which are stabilized by small stiffness parameters. Nevertheless, close results are yielded by S4, S4R5 and the present element using 2×20 elements as well as S9R5 using 1×10 elements. The eigen frequencies computed by Tzou and Ye's element indicates that the element is too stiff.

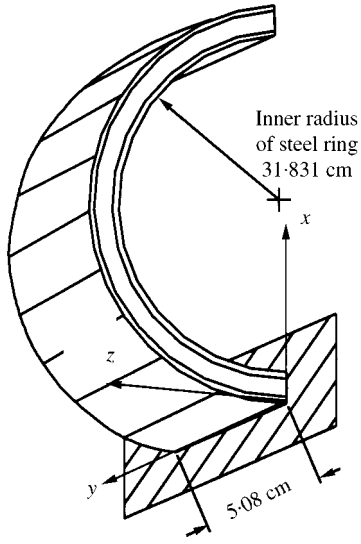

Figure 15. Semi-circular steel ring with surface bonded PZT patches.

TABLE 3

The eigenfrequencies (in Hz) for the steel ring (without the PZT layers) in Figure 15

	Mesh	Mode 1	Mode 2	Mode 3	Mode 4	Mode 5
S4 shell	1×10	3·6552	6·0444	12·301	34·944	44·092
	$2 \times 20^{\dagger}$	3·6920	5·9455	11·965	34·043	41·446
S4R5 shell	1×10	3·2930	3·7298	9·2736	12·102	32·565
	$2 \times 20^{\dagger}$	3·7439	5·9033	11·911	33·342	41·238
S9R5 shell	$1 \times 10^{\dagger}$	3·7475	5·8971	11·856	33·634	40·626
Present	1×10	3·6822	5·8278	11·838	33·641	42·295
	$2 \times 20^{\ddagger}$	3·6810	5·8041	11·691	33·231	40·450
Tzou and Ye [7]	$2 \times 10^{\ddagger}$	8·17	25·66	86·93	194·14	346·08

† Denotes the same number of nodes and d.o.f.s
‡ Denotes the same number of nodes and d.o.f.s.

In the subsequent computations, the ring is modelled by 1×10 elements. A tip circumferential load of 100 N/m is applied along the negative Z direction. The voltage outputs of the 10 piezoelectric elements modelling the inner PZT layer are plotted in Figure 16. The strain is largest at the clamped end and so is the voltage output. The voltage predictions by the solid-shell and membrane piezoelectric elements modelling the inner PZT layer are plotted in Figure 16. The strain is largest at the clamped end and so is the voltage output. The voltage predictions by the solid-shell and membrane piezoelectric elements are graphically indistinguishable except at the vicinity of the clamped end for both thick and thin PZT layers.

The ring shell is then sandwiched by 1 pair (10% of the ring counting from the clamped end is covered) to 10 pairs (100% as covered) of PZT patches. The inner and outer patches serve, respectively, as sensors and actuators which are linked by negative velocity feedback controller(s) of unit gain. Figures 17 and 18 show the damping ratio for the first eigenmode with different numbers of S/A (sensor/actuator) pairs constituted by thick (254 μm) and thin

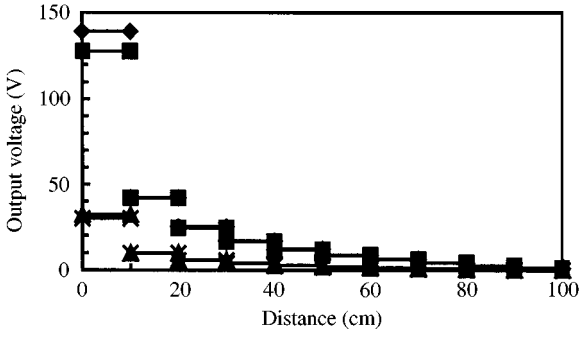

Figure 16. Voltage output of inner PZT layer bonded to the semi-circular ring in Figure 15: —◆— solid, thick PZT; —■— membrane, thick PZT; —▲— solid, thin PZT; —✳— membrane, thin PZT.

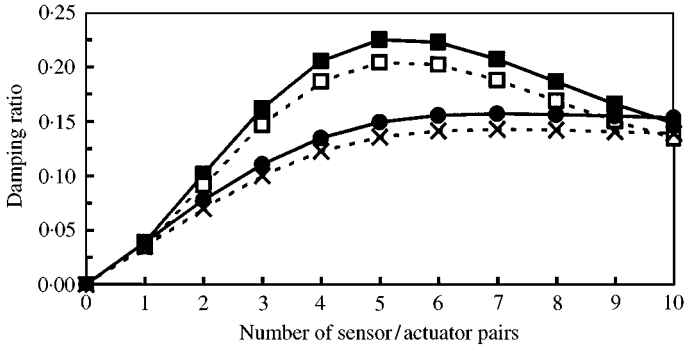

Figure 17. Damping ratio of the ring in Figure 15 versus the number of thick piezoelectric pairs: —■— solid, 1-controller; - - □ - - membrane, 1-controller; —●— solid, multi-controllers; - - × - - membrane, multi-controllers.

(50·8 μm) PZT patches respectively. With only one controller (all sensing patches are electrically connected and so are the actuating patches), the damping ratio increases rapidly from zero S/A pair to four S/A pairs, reaches its peak and starts to drop at five S/A pairs. With multiple controllers where each S/A pair employs a separate controller, the damping ratio increases monotonically with the number of S/A pairs. It is noteworthy that the control effectiveness of using one controller is better than that of using multi-controllers. Comparing Figures 17 and 18, the membrane approximation of the PZT patches is more realistic for the thinner patches.

10.5. SQUARE PLATE WITH SEGMENTED SENSORS AND ACTUATORS

Figure 19 shows a simply supported 1·6 mm thick plexiglass square plate ($\rho = 1190\ \text{kg/m}^3$, $E = 3{\cdot}1$ GPa, $\nu = 0{\cdot}35$) with eight 40 μm thick surface-bonded PVDF films ($\rho = 1800\ \text{kg/m}^3$, $E = 2{\cdot}0$ GPa, $\nu = 0{\cdot}2$, $d_{31} = d_{32} = 10$ pm/V, $\in_{33} = 0{\cdot}1062$ nF/m). The films bonded to the top and bottom faces are used as actuators and sensors respectively [5]. The Plexiglass plate is modelled by 17×17 elements whereas each PVDF film is modelled by 7×7 elements. The gap between the PVDF film is not specified in reference [5] and is here taken rather arbitrarily to be 1/200 of plexiglass length. In the absence of the PVDF films, the eigenfrequencies of the plate are predicted and compared to that obtained

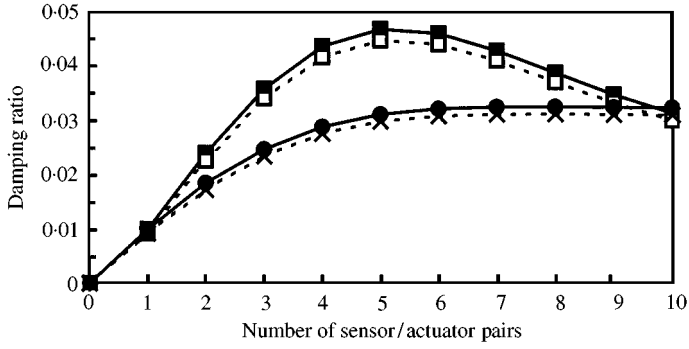

Figure 18. Damping ratio of the ring in Figure 15 versus the number of thin piezoelectric pairs: —■— solid, 1-controller; - - □ - - membrane, 1-controller; —●— solid, multi-controllers; - - × - - membrane, multi-controllers.

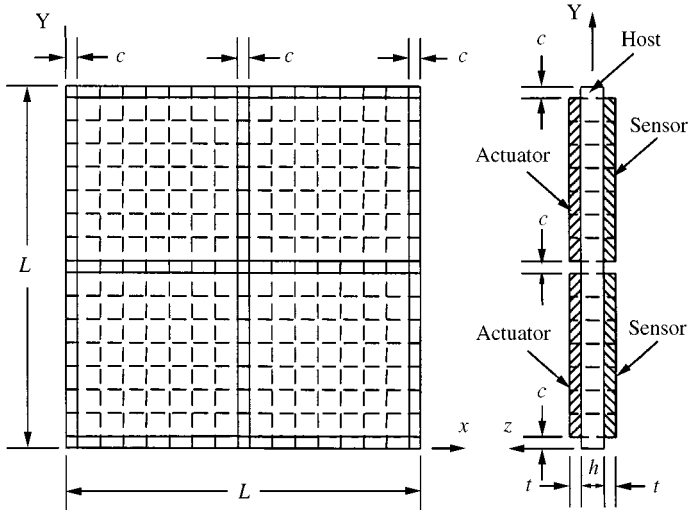

Figure 19. A Plexiglass plate with segmented PVDF piezoelectric sensors and actuators, $L = 400$ mm, $c = 2$ mm, $h = 1{\cdot}6$ mm, $t = 0{\cdot}04$ mm.

by Tzou *et al.*'s solid element. For the purpose of comparison, the frequencies are also computed with the PVDF films included and with a 17×17 uniform mesh. It can be seen from Table 4 that the element of Tzou *et al.* is accurate only for the first mode whereas the present solid-shell element is still reasonably accurate for the third mode. It is noted that Tzou *et al.*'s solid elements [7] and Ha *et al.*'s solid elements [1] are highly similar, if not identical, in the sense that they all contain nine incompatible displacement modes and, thus, exhibit shear locking when the elements are not in the form of rectangular prisms [25].

With the passive damping coefficient of the smart plate taken to be 0·01, the initial deflection of the composite plate structure is prescribed according to the first eigenmode at 1 mm amplitude. The signals from the four sensors are input into four negative velocity feedback controllers which drive the four actuators immediately above the respective sensors. Figure 20 shows the 10 per cent settling time versus the controller gain. As only the first mode is focused, the results predicted by present solid-shell elements and Tzou *et al.*'s incompatible are in good agreement. The PDVF films are also modelled by the piezoelectric

TABLE 4

Eigen frequencies (in Hz) of the simply supported Plexiglass square plate in Figure 19

Modes	$m = 1, n = 1$	$m = 1, n = 2$	$m = 2, n = 2$
Tzou *et al.*, w/o PVDF [7]	15·9	41·7	70·6
Non-uniform mesh w/o PVDF	15·688	39·782	63·681
Uniform mesh w/o PVDF	15·672	39·523	63·263
Non-uniform mesh with PVDF	17·803	40·082	64·132
Series solution [22]	15·524	39·060	62·496

Note: m and n are the numbers of peaks in the eigenmodes along the X and Y directions.

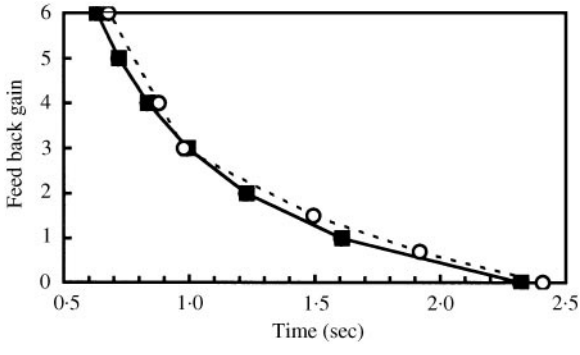

Figure 20. Ten per cent setting time for the Plexiglass plate in Figure 16 versus feedback gains: —●— solid; —■— membrane; - - -○- - - Tzou *et al.* [7].

membrane elements. The prediction is graphically indistinguishable from that of the piezoelectric solid-shell elements by virtue of the fact that the plexiglass is 400 times thicker than the PDVF.

11. CLOSURE

In this paper, a number of finite element models are developed for modelling smart structures with surface-bonded piezoelectric patches. New solid-shell elements for formulated for modelling homogeneous and laminated host structures. The assumed natural strain method is employed to resolve the shear and trapezoidal lockings observed in conventional solid elements whereas the hybrid stress method is employed to improve the inplane element response. Piezoelectric solid-shell and membrane elements are developed by including the electromechanical coupling effect. Unlike the conventional piezoelectric elements, the poling direction of the piezoelectric material is assumed to be parallel to the transverse direction of the elements as it always happens in practice. Moreover, the notion of electric nodes is introduced that can conveniently take into account the equipotential effect induced by the metallization coated on the piezoelectric material. Several examples are examined to illustrate the accuracy and efficacy of the derived models. In particular, the piezoelectric membrane element offers a more economical and convenient choice for modelling thin piezoelectric patches than its solid-shell counterpart.

ACKNOWLEDGMENT

The work described in this paper was substantially supported by an Earmarked Research Grant from the *Research Grant Council of the HongKong SAR, P.R. China* (Project no. HKU 7082/97E).

REFERENCES

1. S. K. HA, C. KEILERS and F. K. CHANG 1992 *American Institute of Aeronautics and Astronautics Journal* **30**, 772–780. Finite element analysis of composite structures containing distributed piezoelectric sensors and actuators.
2. K. CHANDRASHEKHARA and A. N. AGARWAL 1993 *Journal of Intelligent Material Systems & Structures* **4**, 496–508. Active vibration control of laminated composite plates using piezoelectric devices: a finite element approach.
3. W. S. HWANG and H. C. PARK 1993 *American Institute of Aeronautics and Astronautics Journal* **31**, 930–937. Finite element modelling of piezoelectric sensors and actuators.
4. S. S. RAO and M. SUNAR 1993 *American Institute of Aeronautics and Astronautics Journal* **31**, 1280–1286. Analysis of distributed thermopiezoelectric sensors and actuators in advanced intelligent structures.
5. H. S. TZOU, C. I. TSENG and H. BAHRAMI 1994 *Finite Elements in Analysis and Design* **16**, 27–42. A thin piezoelectric hexahedron finite element applied to design of smart continua.
6. D. T. DETWILER, M. H. SHEN and V. B. VENKAYYA 1995 *Finite Elements in Analysis and Design* **20**, 87–100. Finite element analysis of laminated composite structures containing distributed piezoelectric actuators and sensors.
7. H. S. TZOU and R. YE 1996 *American Institute of Aeronautics and Astronautics Journal* **34**, 110–115. Analysis of piezoelectric structures with laminated piezoelectric triangle shell elements.
8. J. KIM, V. V. VARADAN and V. K. VARADAN 1997 *International Journal of Numerical Methods in Engineering* **40**, 817–832. Finite element modelling of structures including piezoelectric active devices.
9. Z. D. WANG, S. H. CHEN and W. Z. HAN 1997 *Finite elements in analysis and design* **26**, 303–314. The static shape control for intelligent structures.
10. C. I. TSENG 1989 *Ph.D. dissertation, University of Kentucky, Lexington, Ky. July*. Electro-mechanical dynamics of a coupled piezoelectric/mechanical system applied to vibration control and distributed sensing.
11. K. Y. SZE, S. YI and M. H. TAY 1997 *International Journal of Numerical Methods in Engineering* **40**, 1839–1856. An explicit hybrid-stabilized eighteen-node solid element for thin shell analysis.
12. K. J. BATHE and E. N. DVORKIN 1986 *International Journal of Numerical Methods in Engineering* **22**, 697–722. A formulation of general shell elements — the use of mixed interpolation of tensorial components.
13. R. H. MACNEAL 1987 *International Journal of Numerical Methods in Engineering* **24**, 1793–1799. A theorem regarding locking of tapered four-node membrane elements.
14. K. Y. SZE 2000 *International Journal of Numerical Methods in Engineering* **47**, 907–920. On immunizing five-beta hybrid stress elements from "trapezoidal locking" in practical analysis.
15. H. S. STOLARSKI 1991 *First U.S. National Congress on Computational Mechanics July* 21–24, *Chicago*. On a formulation of the quadrilateral with highly accurate in-plane bending behavior.
16. T. H. H. PIAN 1985 *Finite Elements in Analysis & Design* **1**, 131–140. Finite elements based on consistently assumed stresses and displacements.
17. K. Y. SZE 1992 *International Journal of Numerical Methods in Engineering* **35**, 1–20. Efficient formulation of robust hybrid elements using orthogonal stress/strain interpolants and admissible matrix formulation.
18. E. P. ERNISSE 1967 *IEEE Transactions on Sonics and Ultrasonics* **14**, 153–160. Variational method for electroelastic vibration analysis.
19. K. Y. SZE and Y. S. PAN 1999 *Journal Sound and Vibration* **26**, 519–547. Hybrid finite element models for piezoelectric materials.
20. H. S. TZOU 1993 *Piezoelectric Shells: Distributed Sensing and Control of Continua*. Netherlands: Kluwer Academic Publishers.
21. *ABAQUS User's Manual* 1998 Version 5.8. Rhode Island: Hibbitt, Karlsson & Sorensen, Inc.
22. A. W. LEISSA 1969 *Vibration of Plates*. Washington D.C.: Scientific & Technical Information Division, NASA.

23. S. P. TIMOSHENKO and S. WOINOWSKY-KRIEGER 1959 *Theory of Plates and Shells*. New York: McGraw-Hill, second edition.
24. J. L. CRAWLY and K. B. LAZARUS 1991 *American Institute of Aeronautics and Astronautics Journal* **29**, 944–951. Induced strain actuation of isotropic and anisotropic plate.
25. K. Y. SZE and A. GHALI 1993 *International Journal of Numerical Methods in Engineering* **36**, 1519–1540. An hexahedral element for plates, shells and beams by selective scaling.
26. K. Y. SZE, L. Q. YAO and S. N. ATLURI in press *Computational Mechanics*. Development of solid-shell elements with particular reference to thickness strain (accepted).

APPENDIX A

By changing the objects of equation (10), the constitutive relation for a generic lamina can be expressed as

$$\left\{\begin{matrix}\boldsymbol{\sigma}_= \\ \cdots \\ \varepsilon_\parallel\end{matrix}\right\} = \left[\begin{matrix}\mathbf{A} & \vdots & \mathbf{B} \\ \cdots & \cdots & \cdots \\ -\mathbf{B}^{\mathrm{T}} & \vdots & D\end{matrix}\right]\left\{\begin{matrix}\boldsymbol{\varepsilon}_= \\ \cdots \\ \boldsymbol{\sigma}_\parallel\end{matrix}\right\} = \left[\begin{matrix}\mathbf{S}_=^{-1} & \vdots & -\mathbf{S}_=^{-1}\mathbf{S}_\times \\ \cdots & \cdots & \cdots \\ \mathbf{S}_\times^{\mathrm{T}}\mathbf{S}_=^{-1} & \vdots & S_\parallel - \mathbf{S}_\times^{\mathrm{T}}\mathbf{S}_=^{-1}\mathbf{S}_\times\end{matrix}\right]\left\{\begin{matrix}\boldsymbol{\varepsilon}_= \\ \cdots \\ \sigma_\parallel\end{matrix}\right\},$$

where

$$\left[\begin{matrix}\mathbf{C}_= & \vdots & \mathbf{C}_\times \\ \cdots & \cdots & \cdots \\ \mathbf{C}_\times^{\mathrm{T}} & \vdots & C_\parallel\end{matrix}\right] = \left[\begin{matrix}\mathbf{S}_= & \vdots & \mathbf{S}_\times \\ \cdots & \cdots & \cdots \\ \mathbf{S}_\times^{\mathrm{T}} & \vdots & S_\parallel\end{matrix}\right]^{-1}$$

$$= \left[\begin{matrix}\mathbf{S}_=^{-1} + \mathbf{S}_=^{-1}\mathbf{S}_\times\mathbf{S}_\times^{\mathrm{T}}\mathbf{S}_=^{-1}/(S_\parallel - \mathbf{S}_\times^{\mathrm{T}}\mathbf{S}_=^{-1}\mathbf{S}_\times) & \vdots & -\mathbf{S}_=^{-1}\mathbf{S}_\times/(S_\parallel - \mathbf{S}_\times^{\mathrm{T}}\mathbf{S}_=^{-1}\mathbf{S}_\times) \\ \cdots & \cdots & \cdots \\ -\mathbf{S}_\times^{\mathrm{T}}\mathbf{S}_=^{-1}/(S_\parallel - \mathbf{S}_\times^{\mathrm{T}}\mathbf{S}_=^{-1}\mathbf{S}_\times) & \vdots & 1/(S_\parallel - \mathbf{S}_\times^{\mathrm{T}}\mathbf{S}_=^{-1}\mathbf{S}_\times)\end{matrix}\right].$$

In order to inhibit thickness locking (also known as Poisson's locking) and recognize the thickness average nature of $\varepsilon_\parallel$ in the element, the modified generalized stiffness matrix for replacing $\mathbf{C}_G$ is derived as [26]

$$\tilde{\mathbf{C}}_G = \begin{bmatrix}\mathbf{A}_0 + \mathbf{B}_0\mathbf{B}_0^{\mathrm{T}}/D_0 & \mathbf{B}_0/D_0 & \mathbf{A}_1 + \mathbf{B}_0\mathbf{B}_1^{\mathrm{T}}/D_0 \\ \mathbf{B}_0^{\mathrm{T}}/D_0 & 1/D_0 & \mathbf{B}_1^{\mathrm{T}}/D_0 \\ \mathbf{A}_1 + \mathbf{B}_1\mathbf{B}_0^{\mathrm{T}}/D_0 & \mathbf{B}_1/D_0 & \mathbf{A}_2 + \mathbf{B}_1\mathbf{B}_1^{\mathrm{T}}/D_0\end{bmatrix}$$

in which

$$[\mathbf{A}_0, \mathbf{A}_1, \mathbf{A}_2, \mathbf{B}_0, \mathbf{B}_1, D_0] = \frac{1}{2}\int_{-1}^{+1}[\mathbf{A}, \zeta\mathbf{A}, \zeta^2\mathbf{A}, \mathbf{B}, \zeta\mathbf{B}, D]\,\mathrm{d}\zeta.$$

For homogeneous materials, the material constitutive coefficients are independent of ζ. Thus,

$$\mathbf{A}_0 = \mathbf{A},\ \ \mathbf{A}_1 = \mathbf{0}_{3\times 3},\ \ \mathbf{A}_2 = \mathbf{A}/3,\ \ \mathbf{B}_1 = \mathbf{0}_{3\times 1},\ \ \mathbf{B}_0 = \mathbf{B},\ \ D_0 = D \text{ and } \tilde{\mathbf{C}}_G = \begin{bmatrix}\mathbf{C}_= & \mathbf{C}_\times & \mathbf{0}_{3\times 3} \\ \mathbf{C}_\times^{\mathrm{T}} & C_\parallel & \mathbf{0}_{1\times 3} \\ \mathbf{0}_{3\times 3} & \mathbf{0}_{3\times 1} & \mathbf{S}_=^{-1}/\mathbf{S}\end{bmatrix}$$

whereas

$$\mathbf{C}_G = \begin{bmatrix}\mathbf{C}_= & \mathbf{C}_\times & \mathbf{0}_{3\times 3} \\ \mathbf{C}_\times^{\mathrm{T}} & C_\parallel & \mathbf{0}_{1\times 3} \\ \mathbf{0}_{3\times 3} & \mathbf{0}_{3\times 1} & \mathbf{C}_=/3\end{bmatrix},$$